







A chemical threshold controls nanocrystallization and degassing behaviour in basalt magmas

Alex Scarani ^{1✉}, Alessio Zandonà ^{2✉}, Fabrizio Di Fiore ¹, Pedro Valdivia³, Rizaldi Putra³, Nobuyoshi Miyajima ³, Hansjörg Bornhöft⁴, Alessandro Vona ¹, Joachim Deubener ⁴, Claudia Romano¹ & Danilo Di Genova⁵

An increasing number of studies are being presented demonstrating that volcanic glasses can be heterogeneous at the nanoscale. These nano-heterogeneities can develop both during viscosity measurements in the laboratory and during magma eruptions. Our multifaceted study identifies here total transition metal oxide content as a crucial compositional factor governing the tendency of basalt melts and glasses towards nanolitization: at both anhydrous and hydrous conditions, an undercooled trachybasalt melt from Mt. Etna readily develops nanocrystals whose formation also hampers viscosity measurements, while a similar but FeO- and TiO₂-poorer basalt melt from Stromboli proves far more stable at similar conditions. We therefore outline a procedure to reliably derive pure liquid viscosity without the effect of nanocrystals, additionally discussing how subtle compositional differences may contribute to the different eruptive styles of Mt. Etna and Stromboli.

¹Dipartimento di Scienze, Università degli Studi Roma Tre, Largo San L. Murialdo 1, 00146 Rome, Italy. ²CNRS, CEMHTI UPR3079, University of Orléans, F-45071 Orléans, France. ³Bavarian Research Institute of Experimental Geochemistry and Geophysics (BGI), University of Bayreuth, Universitätsstraße 30, 95440 Bayreuth, Germany. ⁴Institute of Non-metallic Materials, Clausthal University of Technology, Zehntnerstraße 2a, D-38678 Clausthal-Zellerfeld, Germany. ⁵Institute of Environmental Geology and Geoengineering (IGAG), National Research Council of Italy (CNR), Rome, Italy. ✉email: alex.scarani@uniroma3.it; alessio.zandonà@cnrs-orleans.fr

Volcanic eruptions occur daily—about 100 times per year¹—and some potentially have extreme destructive power as they can release an enormous amount of energy in a very short time. Depending on their size and style (explosive or effusive), volcanic eruptions can alter climate both locally and globally, cause mass extinctions, fatalities, famine and diseases^{2–7}. As such, they represent a serious threat to human activities, infrastructures, and economy. It follows that the probabilistic prediction and mitigation of volcanic risks have acquired paramount importance in modern Earth science. The mechanistic understanding of magma fragmentation and hence explosive behavior of volcanoes represents indeed one of the three grand challenges in volcanology and eruption forecasting⁸.

Probabilistic predictions of volcanic eruptions rely on numerical modeling of magmatic processes^{9–13}. Among the parameters necessary to model eruptive scenarios, those describing magma transport and hence rheology are the most crucial. Magma viscosity is the central parameter that controls rheology and thus the flow behavior from the storage environment to the volcanic vent^{14–19}. In particular, the temperature and chemistry dependence of melt viscosity is key in controlling magma transport, its decompression rate and thereby the overall eruptive style^{20–27}.

Empirical models of melt viscosity^{28–31} are routinely used to approximate magma viscosity under eruptive conditions. These models are based on experimental data obtained over several decades from viscometry measurements (ref. ³¹ and references therein). However, numerous studies have highlighted the challenges associated with accurately determining the viscosity of melts prone to partial crystallization^{21–23,32–35}, which can lead to overestimating the viscosity of the liquid by up to two orders of magnitude^{21,32}. The experiments appear particularly challenging for compositions containing iron and titanium oxides and viscosity values between $\sim 10^9$ and $\sim 10^{12}$ Pa s, where pervasive nanoscale crystallization can easily go undetected if the samples are not checked post-measurement with adequate detection limits and spatial resolution. Given the importance of low-temperature measurements for the extrapolation of both anhydrous and especially hydrous viscosity to eruptive conditions, these experimental difficulties bring into question the accuracy of our present knowledge of the pure liquid viscosity of magmas. This uncertainty necessarily reverberates into numerical modeling of

volcanic eruptions, within which magma viscosity influences dramatically the eruptive scenario.

Here, we demonstrate the experimental challenges related to the correct determination of the viscosity of magmatic liquids, using a multipronged approach that includes viscosity measurements, Raman spectroscopy and transmission electron microscopy. As previously inferred³², near- T_g (the glass transition temperature) nanocrystallization of iron titanium oxides substantially increases the low-temperature viscosity of a Mt. Etna trachybasalt (Italy), while such phenomenon is far less impacting (if not absent) in a Stromboli high-K basalt (Italy) measured at similar conditions. We attribute this difference to small but significant differences in total iron and titanium content, which can dramatically affect the tendency of the magmas to reach oversaturation in the vicinity of T_g and (nano)crystallize. We thereby emphasize the need for a critical review and validation of the published viscosity data, providing a vademecum for correct experimental determination of viscosity based on our previous studies^{32,36}.

However, our results have implications that are potentially further-reaching than the laboratory, since nanocrystals have been identified in various rocks formed during explosive eruptions^{21,32,33,37–51}. Only in the last 4 years, 60 studies^{21,23,31–36,38–112} have been published reporting or inferring the presence of nanocrystals in natural and synthetic samples (Fig. 1). Because the formation of nanocrystals can increase magma viscosity in unexpected ways^{21,32} and trigger vigorous nucleation of bubbles upon magma decompression and undercooling^{46–49,101}, our study aims to stimulate a reappraisal of magma rheology and fragmentation in the possible case of syn-eruptive nanocrystals formation. We initiate this process through the provocative speculation that the peculiarly dissimilar eruptive activities of Mt. Etna and Stromboli (summarized in section “On the eruption styles of Mt. Etna and Stromboli volcanoes”) may also originate from a different degree of undercooling-driven oversaturation in Fe- and Ti-oxides, controlling the tendency of their magmas to (nano)crystallize. High-pressure and -temperature experiments using hydrous melts at eruptive conditions confirm that nanolitization occurs more pervasively in Mt. Etna basalt as compared to Stromboli fostering bubble nucleation. We finally discuss the relevance of our results within the realm of basaltic volcanism.

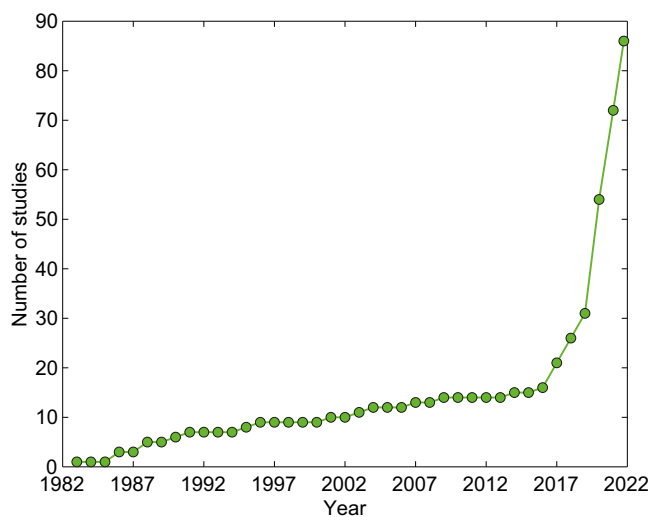


Fig. 1 Literature sources dealing with nanolites. Cumulative number of volcanologically relevant studies either explicitly focusing on nanocrystals or referring to their presence and role in magmatic products and/or in synthetic melts and glasses.

On the eruption styles of Mt. Etna and Stromboli volcanoes.

The recent explosive activity of Mt. Etna is characterized by weak Strombolian eruptions and more energetic paroxysms^{113,114}. The latter consist of lava fountains that can have a duration ranging from several minutes to a few hours and produce eruptive plumes of more than 10 km in height^{115–119}. Lava fountaining at Etna has been interpreted as generated when large volumes of volatiles rapidly exsolve from the magma during its fast ascent and decompression along the conduit^{120,121} producing magma fountains with exit velocities ranging between 33 and 125 m s⁻¹^{122–125}. Recently, it has been suggested¹²⁶ that lava fountaining is a distinct style, separate from effusive and explosive eruption styles, that is produced when magma ascends rapidly and fragments above the vent.

Ordinary activity at Stromboli consists of persistent, rhythmic, mild Strombolian-type eruptions, driven by the bursting of large bubbles called slugs¹²⁷. Ejected pyroclasts are made of degassed and highly porphyritic (phenocryst- and microlite-rich) magma stalling at shallow levels (~ 1 km b.s.l.)¹²⁸. Mechanisms leading to Strombolian eruptions imply slow magma ascent rates (< 0.01 – 0.1 m s⁻¹), permitting significant bubble coalescence to form gas slugs and promote decoupled gas-melt flow²⁷. At

Stromboli, this activity is occasionally punctuated by short-lived, highly energetic explosions, known as paroxysms^{129–131}. These eruptions are characterized by the emission of pyroclasts to a height of a few kilometers above the craters, the production of 3–5 km high eruptive columns and occasionally pyroclastic flows^{132–134}. The triggering mechanism of these paroxysms is still the subject of debate¹³⁵, but there is consensus on the primary role of a deep, volatile-rich aphyric basaltic magma rapidly rising (1–3 m s⁻¹)^{136,137} from the lower magmatic system.

The main difference between the paroxysms of Stromboli and Mt. Etna lies in their duration. While paroxysmal eruptions at Stromboli are single explosions and have a duration of a few minutes¹³², the sustained lava fountaining can persist at Mt. Etna for more than 1 h^{118,120}. As such, Stromboli paroxysms have been recently defined as basaltic Vulcanian eruptions¹³², in which the eruption overpressure is provided by a small amount of volatile-rich magma undergoing closed system degassing, while the shallow crystal-rich viscous magma acts as a weak plug^{138,139}. In contrast, the long duration of lava fountains at Mt. Etna testifies to sustained conditions of coupling between the melt and the gas phases during closed system degassing^{115,126}.

Results and discussion

Near- T_g and superliquidus viscosity measurements were performed on ETN and STR and compared to the whole-curve parameterization based on the Mauro–Yue–Ellison–Gupta–Allan (MYEGA) equation (Eq. (1), ref. 140):

$$\log_{10}\eta = \log_{10}\eta_{\infty} + (12 - \log_{10}\eta) \frac{T_g}{T} \exp \left[\left(\frac{m}{12 - \log_{10}\eta} - 1 \right) \left(\frac{T_g}{T} - 1 \right) \right] \quad (1)$$

where T_g is the glass transition temperature, m the fragility index and $\log_{10}\eta_{\infty}$ the viscosity at infinite temperature, which was fixed equal to -2.9 ± 0.3 in agreement with literature results from materials and Earth sciences^{31,141}.

Low-temperature viscosity measurements of ETN exhibited a physically unrealistic trend and an evident time-dependent increase in viscosity (Supplementary Fig. 2). We therefore used T_g and m derived elsewhere by calorimetry and Brillouin spectroscopy³⁶. Literature data enabled the very accurate description of high-temperature concentric-cylinder data (Fig. 2a). In the case of STR (Fig. 2b), T_g and m were fit to our viscosity data measured at both low- and high-temperature (Fig. 2b), retrieving values in good agreement with previous studies (e.g. ^{131,142}, $m = 42.0$ and $T_g = 643.9$ °C). Low-temperature viscosity measurements performed on STR remarkably ran stable up to ~ 780 °C (Supplementary Fig. 2 in the attached Supplementary Data 1). Above this temperature, we observed a slight increase in viscosity over the timescale of the measurement (i.e., 20 min). We subsequently investigated the origin of the observed time-dependent increase in viscosity during micropenetration (MP) measurements by Raman spectroscopy.

The Raman spectra (Fig. 3) of ETN and STR starting materials were typical for basalt glasses^{143,144}. Post-run samples manifested instead a gradual dwindling of the high-wavenumber envelope (> 800 cm⁻¹) associated with the stretching vibrations of oxygens in the silicate network¹⁴⁵. Additional intensity emerged at ~ 300 and ~ 660 cm⁻¹, where the main peaks of Fe-Ti-oxides such as magnetite are most typically observed^{32,146}; these Raman bands appeared already at 640 °C in ETN and intensified at higher temperatures, while they were only visible in STR after the MP measurements performed at the highest temperatures, namely 777 and 797 °C.

DSC upscans performed at 30 K min⁻¹ further confirmed the inferred higher susceptibility of ETN to near- T_g crystallization (Fig. 4). The endothermic glass transition of ETN (onset at 653 °C) was closely followed (after ~ 100 °C) by two distinct exothermic events: a first broad peak with onset at 758 °C and a second, sharper and more intense one with a maximum at 860 °C. After that, the sample melted over a broad endotherm with an offset at 1228 °C. In contrast, STR proved to be much more stable against crystallization: we observed in this sample a single broad exothermic event starting at 963 °C, i.e., ~ 285 °C above its glass transition (onset at 679 °C); the subsequent melting process was completed at 1251 °C. The behavior of ETN closely resembled that of synthetic melts in which the early precipitation of nano-sized TiO₂-bearing seeds is exploited to control the subsequent heterogeneous nucleation of aluminosilicate crystals, as for the production of conventional glass-ceramics¹⁴⁷.

We subsequently subjected ETN to four heat treatments (heating and cooling rates = 10 K min⁻¹) respectively up to 684 °C (ETN+1), 693 °C (ETN+10), 708 °C (ETN+25) and 732 °C (ETN+50), using a DSC for higher temperature precision (see also Supplementary Fig. 3 and Section 3.3). These temperatures are located only slightly above the previously determined T_g of 641 °C³⁶, where viscosity $\eta = 10^{12}$ Pa s; the total time spent above this temperature ranged between 8 and 18 min. The Raman spectra of the obtained samples (Supplementary Fig. 4) exhibited nonetheless similar features to those in Fig. 3, namely the emergence of the Raman signatures for Fe-Ti-oxides at ~ 300 and ~ 660 cm⁻¹^{32,146}. We thereafter characterized these materials also by (S)TEM, to directly assess their nanostructural modification.

TEM imaging confirmed that the homogeneous ETN starting material (Supplementary Fig. 5) developed an increasingly heterogeneous nanostructure during the heat treatments (Fig. 5). Even before the identification of nanocrystals with well-defined lattice fringes in ETN+50, the amorphous silicate matrix of ETN+1, ETN+10 and ETN+25 exhibited the clear emergence of high- and low-contrast regions with a size below 10 nm, hinting at an incipient compositional reorganization of the samples before crystal nucleation. Notice that such features would go undetected by X-ray diffraction and scanning electron microscopy, due to the lack of long-range order and the small size. High-angle annular dark-field (HAADF) micrographs and EDS mappings in STEM mode (Fig. 6) strengthened these observations: Fe, Al and Ti extensively clustered into a channel-like nanostructure already in sample ETN+10, subsequently giving rise to the formation of Fe-, Ti- and Al-bearing nanocrystals and a SiO₂-enriched amorphous matrix in ETN+50. The local SiO₂ enrichment of the matrix around nanocrystals reproduced the formation of diffusion barriers and core-shell nanostructures recently observed in synthetic and natural melts undergoing non-isochemical crystallization^{32,47,147–154}.

A chemical threshold between Mt. Etna and Stromboli. We have shown that an anhydrous trachybasaltic melt from Mt. Etna is substantially more prone to (nano)crystallization than a similar material from Stromboli, as evident from the metastability diagrams sketched in Fig. 7 based on this work and previous literature sources^{47,155}. These dissimilar responses to a dwell at temperatures above T_g must necessarily originate from inherent differences between the samples, i.e., their composition. A quick comparison reveals that ETN contains $\sim 80\%$ more TiO₂ than STR (1.67 \pm 0.05 wt.% and 0.92 \pm 0.10 wt.%, respectively) and $\sim 30\%$ more FeO_{tot} (10.05 \pm 0.17 wt.% and 7.58 \pm 0.25 wt.%, respectively), with only minor discrepancies in the other oxides. This higher content in transition metal oxides is likely to be responsible for the stronger tendency of Mt. Etna trachybasalt

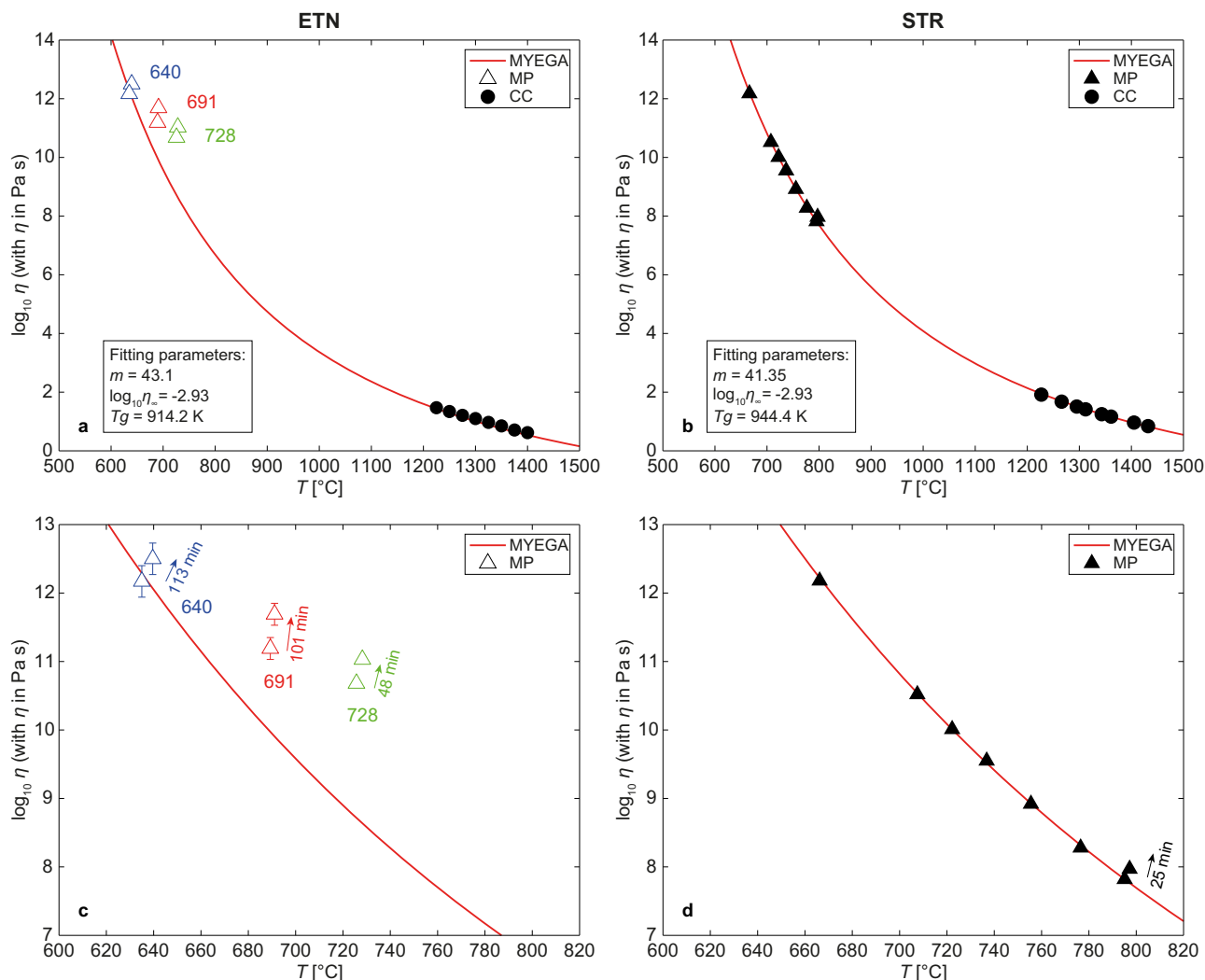


Fig. 2 Viscosity measurements of Mt. Etna and Stromboli basalts. Viscosity measurements performed by micropenetration viscometry (MP; low-temperature range) and rotational viscometry (CC; high-temperature range) on **a** ETN and **b** STR melts, compared to the complete viscosity curves of the pure melts. The low-temperature range is shown in higher detail in panels **(c)** and **(d)**, manifesting the much wider temperature interval in which STR was reliably measurable, whereas ETN invariably exhibited a time-dependent increase in viscosity and a strong deviation from the expected values (see also Supplementary Fig. 2). Red lines correspond to the MYEGA fit using Eq. (1). Error bars correspond to the standard deviations of MP measurements. Where not reported, error bars are smaller than symbols.

toward nanocrystallization; although these components can be assumed to be homogeneously distributed in the stable melt, their solubility in the undercooled liquid is strongly temperature-dependent and is additionally affected by changes in oxygen fugacity^{156–162}. A sufficiently long dwell at medium-to-deep undercooling can therefore induce nucleation and growth of Fe-Ti-oxide crystals simply due to their melt oversaturation, which will ultimately be more pronounced in a FeO- and TiO₂-richer melt. This explanation is supported by fundamental studies of devitrification and crystal nucleation in aluminosilicate melts containing nucleating agents (e.g., TiO₂ and ZrO₂): differences by only a few wt.% typically mark the transition between unchallenging glass quenchability and extensive crystal precipitation^{163,164}.

Nanocrystallization and magma dynamics: moving forward.

Our study signals that nanocrystallization may have a non-negligible and far-reaching impact on magma flow properties, although our observations were gathered in the laboratory during DSC or micropenetration measurements, i.e., upon heating of a

vitriified melt. Similar scenarios would therefore seem to verify only sporadically in nature, such as during the reheating of a solidified plug due to the ascent of hot magma in a volcanic conduit. Nonetheless, it was recently demonstrated that nanocrystals can also precipitate as a result of fast magma undercooling from eruptive temperatures followed by an isothermal dwell (Fig. 7a) in the order of seconds⁴⁷. These observations suggest that nanocrystallization may occur before or after fragmentation and, in fact, recent detailed studies of volcanic deposits go in this direction^{44–46,104}.

Experimental studies and observations of natural products suggest that Fe-Ti-bearing nanolite formation can moreover favor gas-melt coupling by (i) fostering bubble nucleation^{47–49,65,110,111} and (ii) inhibiting gas bubble motion, coalescence and eventually outgassing due to the formation of aggregates and to an increase in viscosity^{21,32,103}. The likelihood of these processes is also supported by studies performed on microlites: it is well known^{165–168} that Fe-Ti-oxides are unrivaled in their ability to facilitate bubble nucleation⁶⁵. Previous melt decompression experiments produced aggregates of bubbles and oxide

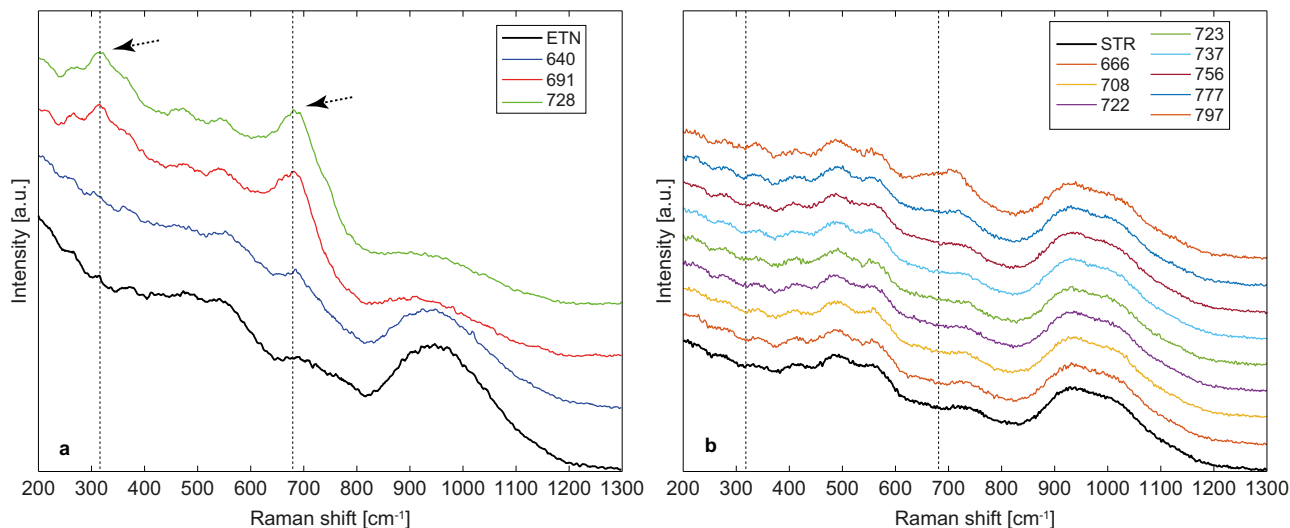


Fig. 3 Post-micropenetration Raman spectra reveal nanocrystallization. Raman spectra collected after micropenetration viscometry: **a** ETN and **b** STR. Numbers in the legend indicate the temperature (°C) of the viscosity measurement. The intensity of Raman spectra increases at ~ 300 and ~ 660 cm^{-1} and decreases at >800 cm^{-1} when Fe-Ti-oxides developed during the viscosity measurements, as highlighted by arrows and vertical dotted lines. This occurred for all ETN samples and for only two STR samples measured at the highest temperature (777 and 797 °C).

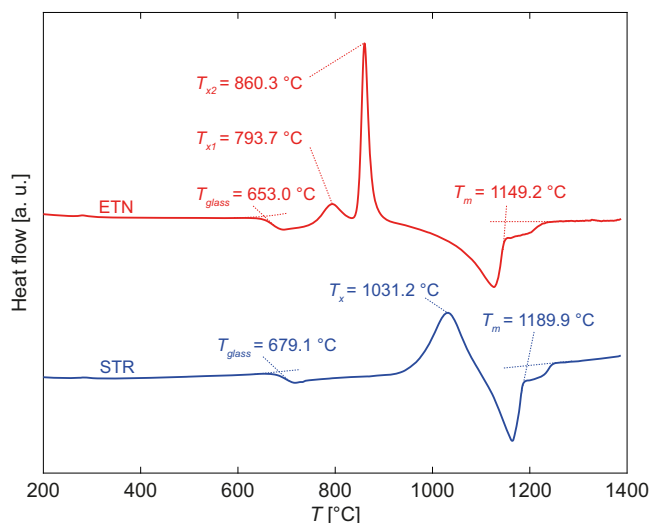


Fig. 4 DSC upscans documenting a different crystallization behavior for ETN and STR glasses. DSC upscans performed at 30 K min^{-1} using ETN and STR samples. Labels: T_{glass} for the glass transition interval, T_{x1} and T_{x2} for exothermic crystallization events, T_m for the melting endotherm.

crystals, which coated part of the outer bubble surfaces in a shell-like morphology¹⁶⁹. It was also found⁸⁵ that the transition from effusive to explosive eruptions occurs at the ascent rates which overlap with those at which new Fe-Ti-oxides are nucleated in the conduit. Recently, bubble number density values in pyroclastic samples from a wide range of Plinian eruptions were consistently associated with heterogeneous nucleation on Fe-Ti-oxides¹⁰¹. It thus appears that eruption styles can be also controlled by the formation of Fe-Ti-oxides, acting as nucleation sites for syn-explosive vesicles in the shallow conduit, thereby triggering magma dehydration and a dramatic increase in viscosity.

So far, we have demonstrated that small differences in the anhydrous composition of basalts control the nanocrystallization of Fe-Ti-oxides. Transferring our findings to a broad range of eruptive scenarios requires the investigation of hydrous magma at

eruptive temperatures and pressures. This led us to an additional series of experiments mimicking conduit conditions, where basalts can be subjected to rapid decompression and cooling during explosive eruptions^{126,170,171}. Starting from superliquidus temperatures (≥ 1250 °C) and stable confining pressures (≥ 400 MPa) in an end-loaded piston cylinder apparatus (see Methods), hydrous basalts from Mt. Etna and Stromboli were subjected to rapid cooling down to the fictive temperature (at $\sim 20 \text{ K s}^{-1}$) that also induced a rapid decompression (< 100 MPa). The microstructures of the products retrieved after the experiments are shown in Fig. 8 and revealed a remarkably different response between the two magmas. At initial pressure of 1000 MPa and water content of 1.68 wt.% for ETN and 4.10 wt.% for STR (determined post-run by FTIR), ETN matrix intensively nanocrystallized (Supplementary Fig. 6) and exhibited nucleation of pyroxene microlite clusters at SEM scale (Fig. 8a), while STR was quenchable as a homogeneous glass (Fig. 8b). Therefore, although the STR melt dissolved significantly more water, and thus is expected to be less viscous than the ETN melt, it was possible to quench the melt as a pure glass. In a second experiment, we increased the dissolved water content to ~ 6 wt.% for both melts and lowered the initial pressure to 400 MPa. Here, degassing and devitrification took place in both melts, although the obtained microstructures were markedly different. The groundmass of ETN 6.30 wt.% H_2O (nominal, we estimated water content as ≥ 4.5 wt.% by Raman spectroscopy) was scattered with nanolites and far richer in bubbles (Fig. 8c), whose irregular shapes (Fig. 8e) suggest deformation due to the high viscosity of the residual melt; conversely, STR 5.93 wt.% H_2O (determined post-run by FTIR) exhibited (Fig. 8d) rounded bubbles occasionally associated to rosettes of acicular microlites (Fig. 8f), in a crystal-free residual glassy phase as confirmed by Raman spectroscopy analysis (Supplementary Fig. 6). It is worth noting that the Raman spectrum of the sample ETN 6.30 wt.% H_2O shows a relatively sharp shoulder at ~ 3650 cm^{-1} of the water region (2700–4000 cm^{-1}). It would thus appear that the formation of nanolites depletes the melt from structurally bonded water to form quasi-crystalline domains and thus further increases magma viscosity. This agrees with recent findings⁴¹ suggesting that the formation of isolated $\text{Fe}(\text{OH})_2$ cluster could occur in iron-rich Martian basalts.

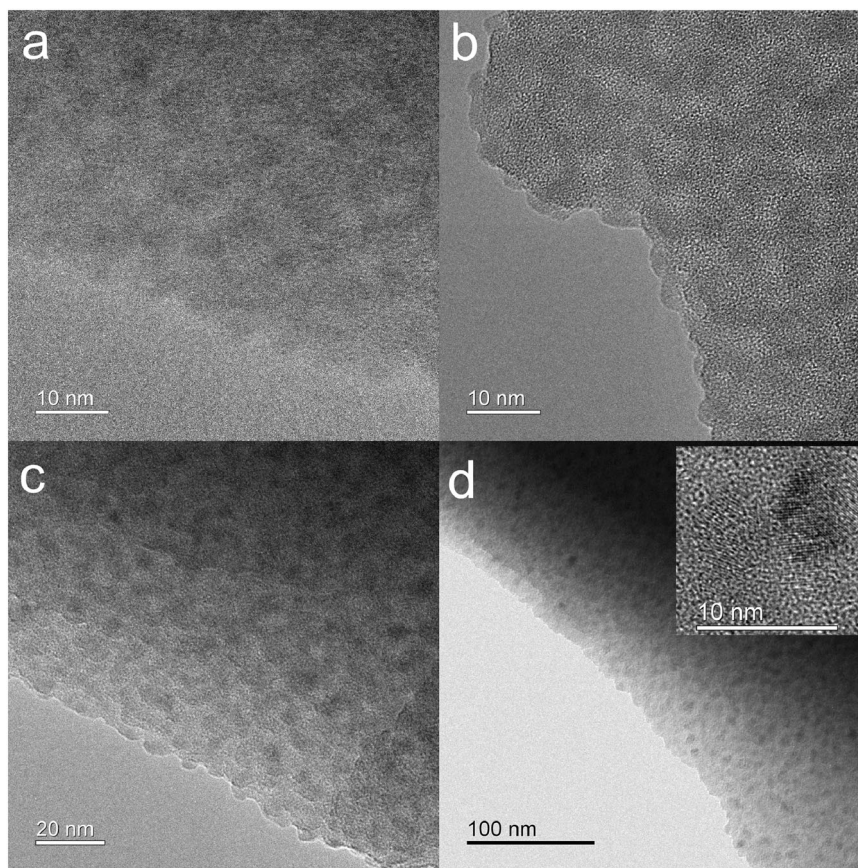


Fig. 5 High-resolution TEM micrographs of nano-heterogeneities and nanocrystals in ETN sample. High-resolution TEM micrographs collected from samples: **a** ENT+1, **b** ETN+10, **c** ETN+25 and **d** ETN+50, with an inset at higher magnification detailing the presence of nanocrystals with well-visible lattice fringes. Mind the different magnification levels, scale bars are provided on each figure.

We therefore hypothesize here that a different tendency toward nanolite formation and gas-melt coupling could play a key role in modulating different eruptive styles during paroxysmal events at Mt. Etna and Stromboli volcanoes. As we reported above, Stromboli paroxysmal explosions are typically short-lived events driven by the eruption of a volatile-rich magma (as compared to the typical low-energy Strombolian activity) undergoing closed system degassing. Conversely, Mt. Etna paroxysms are characterized by long-standing lava fountaining, in which the coupling of melt and bubbles is sustained for hours during magma ascent and degassing: such conditions may be favored by the nanostructuring of Etnean magmas demonstrated in this work. Indeed, scoria produced during fountain-fed activity at Mt. Etna¹⁷² provided textural evidence supporting a marked vesicle size polydispersity (large and small size populations). Notably, while large vesicles result from deep volatile exsolution, the small vesicle population has been interpreted as due to syn-eruptive nucleation¹¹⁵. We furthermore speculate that Fe-Ti-oxide nanolites may prevent efficient bubble coalescence during magma ascent. This effect would hinder the achievement of the percolation threshold¹⁷³ where the system transitions from closed- to open-system degassing¹⁷⁴, or at least limit the formation of efficient permeable pathways¹⁷⁵, ultimately inhibiting gas-melt decoupling (i.e., out-gassing). The sustained fountaining activity at Mt. Etna would be therefore maintained by the eruption of coupled gas-melt mixtures, where the increase of magma viscosity may sustain the over-pressure of the expanding bubbles, continuously accelerating and eventually fragmenting by inertia above the vent^{126,176}. In contrast, the transient short-lived explosive paroxysms at Stromboli are likely to arise due to easier bubble coalescence, also because their

magma is drastically less prone to syn-eruptive nanocrystallization: consequently, the conditions for sustained lava fountaining cannot be reached. Because relatively high iron and titanium content also appears to be a common feature of several highly explosive basaltic eruptions, such as Masaya triple layer and Fontana lapilli (Nicaragua), Etna 122 BC, Tarawera 1886 (New Zealand) and Curacautín ignimbrite (Llaima volcano, Chile)^{177–182}, we propose that chemical composition and more specifically transition metal oversaturation can play a key role in the dynamics of explosive volcanism not only for the cases studied in this work.

To support these speculations, future investigations should be directed toward the exploration of nanoscale magma dynamics at representative temperatures and pressures for eruptive conditions. This will require inter alia the conception of novel experimental facilities^{171,183,184}, at best combined with synchrotron radiation⁴⁷ to allow in situ observations at timescales and with instrumental resolutions otherwise inaccessible in the laboratory.

Nanocrystallization and viscosity measurements: challenges and best practices. Our results manifest the inherent challenges related to the experimental determination of low-temperature viscosity in the case of magmatic melts, typically prone to phase separation, crystallization, or other compositional modifications (e.g., partial dehydration in water-bearing materials) during measurements in the vicinity of T_g . Measurements performed on a heterogeneous sample will yield incorrect viscosity values up to two orders of magnitude, amplifying the uncertainties related to the numerical modeling of magmatic processes and therefore deteriorating our ability to efficiently predict the style of volcanic eruptions from a probabilistic point of view. Because sample

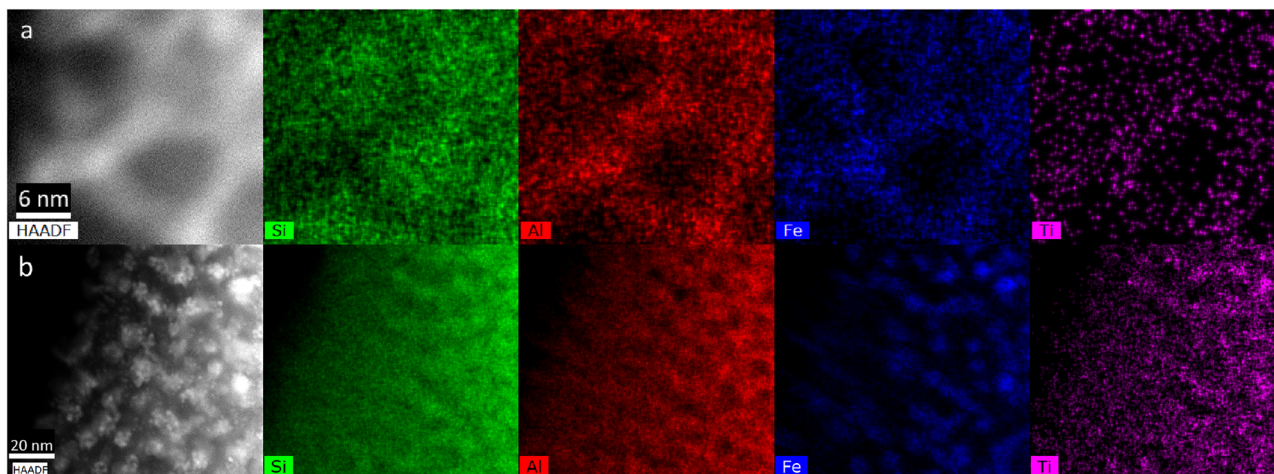


Fig. 6 STEM-HAADF micrographs and EDS-elemental maps, demonstrating nanoscale clustering of Fe, Ti, and Al. STEM-HAADF micrographs and EDS-elemental maps of samples: **a** ETN+10 and **b** ETN+50, detailing the heterogeneous distribution of Si, Al, Fe and Ti at the nanoscale. Mind the different magnification levels, scale bars are provided.

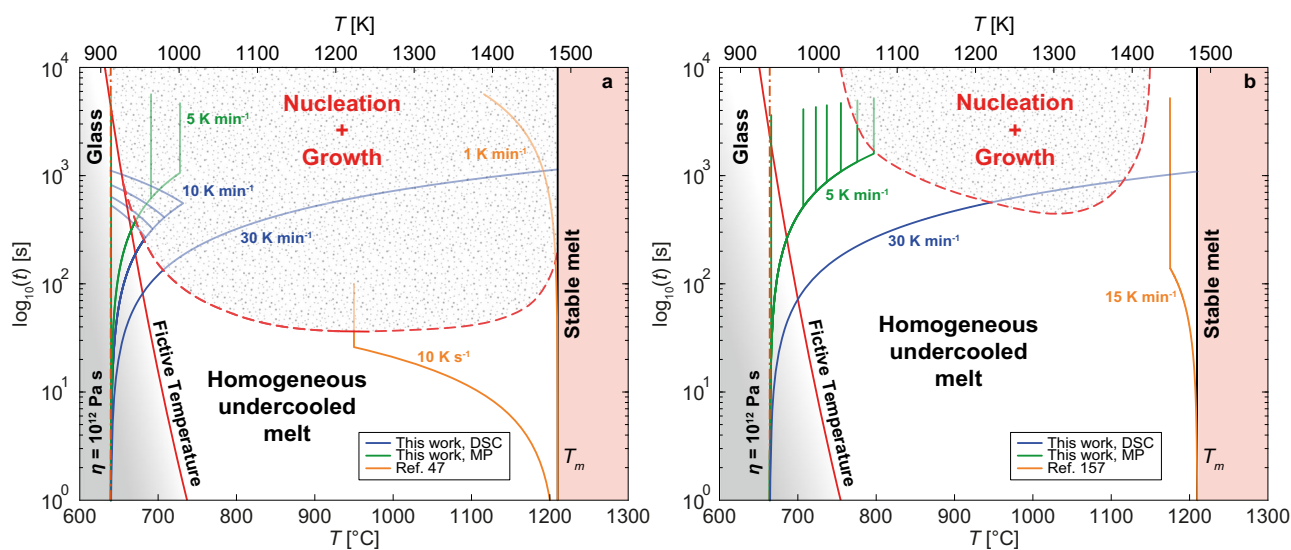


Fig. 7 Metastability diagrams of anhydrous basalts from Mt. Etna and Stromboli. Metastability diagrams of anhydrous basalts from **a** Mt. Etna and **b** Stromboli, providing the approximate timescales and temperatures at which heterogeneities/crystals are detected during laboratory experiments performed at ambient pressure within this work and in some relevant literature sources^{47,155}. Only time spent above T_g and below T_m during heating and cooling experiments is considered here, since no crystals are expected to form outside these boundaries (at least at such relatively short timescales); similarly, the effect of oxygen fugacity is disregarded. The textured fields delimited by red dashed lines signal the onset of nucleation and/or crystal growth in the homogeneous undercooled melts; we provide fictive temperature trends to approximate the role of melt relaxation in the two systems.

instability is a complex function of melt composition and measuring conditions, it can only be qualitatively evaluated beforehand and must be continuously minimized using a sound experimental approach. We propose here below a vademecum based on our experiences in the lab:

- Check the glass homogeneity before the measurements: Raman spectroscopy and TEM are valuable probes to verify the absence of amorphous heterogeneities or Fe-Ti-oxide crystals in starting materials³². Be aware that these nanostructures may be invisible to X-ray diffraction and scanning electron microscopy, due to their small size and lack of long-range order. If the glass is heterogeneous, try to remelt it at higher temperatures and/or quench it faster.
- Always check samples after the measurements as shown here. A quick comparison between the Raman spectrum of

the starting material and those of measured samples can reveal incipient phase separation, the appearance of crystals or a partial loss in volatile components.

- If the sample does not exhibit evident signs of crystallization during the measurements (as Stromboli basalt in this work), the viscosity measurements can be performed using conventional methods (such as micropenetration, beam bending, parallel plate, fiber elongation), involving a long dwell time (tens of minutes) above T_g .
- If the viscosity of the sample changes during isothermal measurements and/or if post-measurement analyses reveal material modifications, a more conservative approach should be preferred: one can still derive viscosity from (flash) calorimetry measurements using the rate matching method, as described elsewhere^{32,77,185,186}. Despite the need for melt relaxation, minimize the temperature

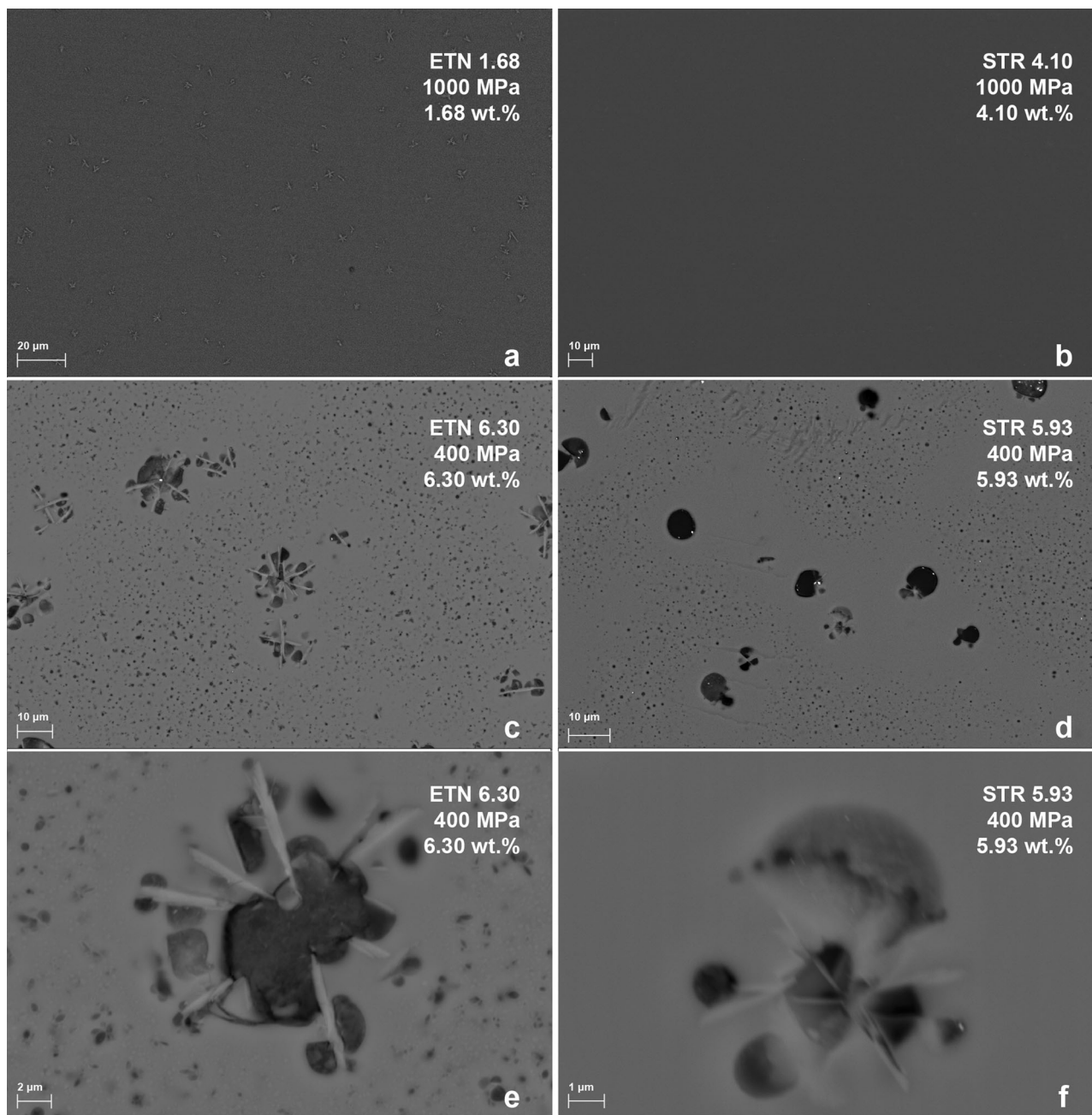


Fig. 8 Backscattered electron (BSE) images of experimental groundmasses obtained from high-temperature and -pressure experiments. Left column: BSE images of ETN samples with measured 1.68 wt.% H₂O by FTIR (**a**) and nominal 6.30 wt.% H₂O (**c** and **e**). Right column: BSE images of STR samples with measured 4.10 wt.% (**b**) and 5.93 wt.% H₂O (**d** and **f**). Pressure used for the syntheses is reported on the figure, with temperature ranging between 1250 and 1300 °C. See Methodology for more details.

excursion above the glass transition during the measurements.

- For particularly unstable samples (such as Mt. Etna basalt in this work), the liquid viscosity curve can be parameterized with sufficient accuracy using T_g derived via DSC (running a measurement with matching rates at 10 K min⁻¹) and a fragility index m obtained from Brillouin spectroscopy³⁶.

Conclusions

Our study demonstrates that a simple dwell above the glass transition temperature on a timescale typical for viscosity measurements can induce the formation of nanocrystals in volcanic

melts. Our results confirm that the formation of amorphous nanostructures and nanocrystals significantly increases the viscosity of volcanic melts up to 2 log units. This phenomenon is assumed to arise due to the compositional evolution of the residual melt, the formation of highly viscous amorphous nanoshells and possibly the agglomeration of nanocrystals. We therefore provide a vademecum for the correct experimental determination of melt viscosity, stressing the need to verify the nanoscale changes that may have occurred in the samples during the measurements.

Our study also has implications for the eruptive dynamics of magmas. Within the compositional domain of basalts, we identify a key chemical parameter, i.e., TiO₂ and FeO_{tot} content: while

Mt. Etna trachybasalt is rich in transition metal oxides and extremely prone to nanocrystallization, Stromboli basalt is a far more stable melt. Because these magmas are involved in two different eruptive styles, we hypothesize that their different nanoscale dynamics may participate in controlling magma degassing and thus the eruptive dynamics of the two volcanoes.

Methods

Starting materials. We used a trachybasaltic lava rock from the 2001 Mt. Etna eruption, Italy¹⁸⁷ and a high-K basaltic pumice sample erupted during the March 15, 2007 paroxysmal event of Stromboli volcano, Italy^{15,188}. The rock samples were crushed using a jaw crusher and a ring-mill and melted in a Fe-saturated Pt crucible at 1400 °C for 2 h. The melts were rapidly quenched to glasses.

The chemical composition of the starting glasses is reported as oxides concentration in Supplementary Table 1 and was determined using a JEOL-JXA8200 electron microprobe at the Bayerisches Geoinstitut (University of Bayreuth, Germany). The chemical analyses were carried out at 15 kV acceleration voltage and 5 nA beam current; a defocused 10 μm beam was used for all elements. Calibration standards were synthetic wollastonite for Ca and Si, periclase for Mg, hematite for Fe, spinel for Al, natural orthoclase for K, and albite for Na. Sodium and potassium were analyzed first to prevent alkali migration effects³⁹. The homogeneity of the samples was tested by measuring the chemical composition at twenty different points across the surface, before and after micropenetration viscometry.

Viscometry. The high-temperature superliquidus viscosity of Mt. Etna's trachybasalt (ETN, 1225 °C < T < 1400 °C, $10^{1.47}$ Pa s > η > $10^{0.62}$ Pa s) was measured using a Rheometric II Rotational Viscometer (Theta Instruments) and a concentric-cylinder geometry at the Experimental Volcanology and Petrology Laboratory (EVPLab, Roma Tre University, Italy). The apparatus is equipped with an Anton Paar Rheolab Qc viscometer head (full-scale torque of 75 mN m). Temperature was monitored using a factory-calibrated S-type thermocouple (precision of ± 2 °C¹⁸⁹) placed near the crucible walls. Accuracy in viscometry measurements was better than 0.06 log units¹⁹⁰. The melt was stirred at a shear rate ($\dot{\gamma}$) of 10 s⁻¹ with a Pt80Rh20 spindle (3.2 and 42 mm in diameter and wetted length, respectively) in air at 1 atm and 1400 °C for 5 h to ensure thermo-chemical homogenization. Subsequently, the temperature was lowered with steps of 25 °C down to 1225 °C, each time waiting until steady temperature and viscosity values were attained (~45 min). At the end of the measurement, the spindle was extracted, and the sample contained in the crucible (volume: ~15 cm³) was allowed to quench in air under continuous water flow to the crucible walls at ~120 K min⁻¹ (ref. 191).

The high-temperature superliquidus viscosity of Stromboli's basalt (STR, 1227 °C < T < 1432 °C, $10^{1.92}$ Pa s > η > $10^{0.84}$ Pa s) was measured using concentric-cylinder viscometry (Haake RV 20, Karlsruhe, Germany) at the Institute of Non-Metallic Materials (TU Clausthal, Germany). The torque reading of the device was calibrated at strain rates from 0.1 to 96 s⁻¹ using the standard DGG-1^{192,193} and the error in viscosity was found to be ± 0.02 log₁₀ units.

The post-run ETN and STR samples were drilled and crushed to obtain samples for the other analytical examinations.

We subjected doubly polished glass disks (3 mm thick) of ETN and STR samples to low-temperature micropenetration viscometry measurements (MP). ETN viscosity was measured at 640, 691 and 728 °C, whereas STR viscosity was measured at ten different temperatures (Supplementary Table S2) ranging from 662 to 797 °C. We used a vertical dilatometer (Bähr VIS 404) at TU Clausthal. The setup consists of a SiO₂ rod pushing a sapphire sphere of radius $r = 0.75$ mm, under a constant Ar flow. When measuring viscosity below 700 °C, we applied a force of 3.92 N (400 g load); we decreased the force (N) to 1.96 (200 g load), 0.98 (100 g load), 0.49 (50 g load), 0.15 (15 g load) and 0.05 (5 g load) to measure viscosity at higher temperatures. The temperature was controlled with an S-type thermocouple (Pt-PtRh) placed at ~2 mm from the sample surface. The temperature error is estimated at ± 5 °C considering the accuracy of the S-type thermocouple and its distance from the sample¹⁹⁴. We followed standard procedures¹⁹⁵ to achieve thermal equilibration of the sample at the target measuring temperature: a heating rate of 0.17 K s⁻¹ (10 K min⁻¹) was imposed up to 100 °C less than the desired temperature, which was then approached with a slower heating rate of 0.08 K s⁻¹ (5 K min⁻¹). After reaching the final dwell temperature, the samples were allowed to relax for approximately ~60–600 s before the load was applied. The indentation depth of the sapphire sphere into the sample was measured as a function of time using a linear variable displacement transducer and viscosity was determined according to the literature¹⁹⁶. We estimated the measurement accuracy by measuring the viscosity of the standard glass DGG-1: the certified viscosity data¹⁹² were reproduced with a standard deviation of ± 0.1 in log units.

Differential scanning calorimetry. Amorphous shards of ETN and STR (mass: ~20 ± 5 mg) were subjected to controlled heat treatments in a differential scanning calorimeter (DSC, 404 F3 Pegasus, Netzsch) at the EVPLab and at TU Clausthal, in PtRh20 crucibles and under N₂ 5.0 atmosphere (25–80 ml min⁻¹ flow rate). The

instruments were calibrated using melting temperatures and enthalpy of fusion of reference materials (pure metals: In, Sn, Bi, Zn, Al, Ag, and Au) up to 1610 °C.

First, we performed a simple upscan at 30 K min⁻¹ for both ETN and STR materials, to gain insight into their general crystallization behavior. We then subjected ETN glass to controlled heat treatments within its glass transition interval: we heated at 10 K min⁻¹ up to either 1, 10, 25 or 50 K above the emergence of T_{peak} (Supplementary Fig. 1) in the heat flow curve, defined as the signal undershoot (exothermic = positive value) after the onset of the glass transition T_{onset} (Supplementary Fig. 1)^{32,77,94,197,198}; we subsequently cooled the material down to room temperature at 10 K min⁻¹ (Supplementary Fig. 2). The samples are hereafter named ETN+1, ETN+10, ETN+25 and ETN+50, respectively. These DSC upscans at 10 K min⁻¹ incidentally confirmed the homogeneity of our starting material and the reproducibility of our experimental procedure, since we obtained from the heat flow curves an average T_{onset} of 644.8 ± 0.7 °C and an average T_{peak} of 682.2 ± 0.5 °C over all four samples analyzed (Supplementary Table 2).

Raman spectroscopy. The samples were characterized before and after DSC and micropenetration measurements using confocal Raman imaging microscopes at the Institute of Non-Metallic Materials (alpha300R, WITec GmbH). The Raman microscope is equipped with a 100× objective, a 532 nm diode green laser (532 nm) and a CCD detector. The integration time employed with the alpha300R microscope was 7 s (3 accumulations, 13 mW laser power). Raman spectra were invariably collected from cracked or polished samples, to exclude possible surface effects. Spectra were acquired in the range from 200 to 1300 cm⁻¹. The Raman spectrometer was calibrated using a silicon standard.

Transmission electron microscopy (TEM). High-resolution TEM micrographs were collected from powdered samples using Phillips CM20FEG and FEI Titan G2 80-200S/TEM microscopes. The analysis in scanning transmission electron microscopy (STEM) mode was carried out using a FEI Titan G2 80-200S/TEM (Bayerisches Geoinstitut, University of Bayreuth, Germany), operated at 200 kV and equipped with an energy-dispersive X-ray spectrometer (EDS) system consisting of four silicon drift detectors (Bruker, QUANTAX EDS).

Synthesis of hydrous samples and decompression experiments. Water was dissolved in the anhydrous melts under pressure and temperature, in an end-loaded piston cylinder apparatus at the Bayerisches Geoinstitut (University of Bayreuth, Germany). The anhydrous and homogenous glasses were crushed and sieved to obtain two size fractions of <100 and 100–250 μm. The two fractions of powder were mixed in a 1:1 ratio and loaded with known amounts of distilled water in Au₈₀Pd₂₀ capsules of 12 mm length, 4.6 and 5 mm of inner and outer diameter, respectively. The anhydrous glass powders and water were added in a stepwise fashion to achieve a homogeneous distribution of water. A metal piston was used to compact the glass powder at each step. The capsules were sealed by arc welding. The capsules were weighed before and after being placed in an oven at 110 °C for at least an hour to ensure that water was unable to escape. The syntheses were performed between 400 and 1000 MPa and 1250–1300 °C for 24 h using a 3/4 talc-pyrex-Al₂O₃ assembly and a graphite furnace. Heating was performed at 100 K min⁻¹, while pressure was adjusted manually to the target value through an upper 500-bar ram and a lower ram, it was set to automatic control once the target pressure and temperature values were achieved. Temperature was measured by a type S thermocouple (Pt₉₀Rh₁₀) and a friction correction was applied based on calibrations^{199,200}. The runs were terminated by turning off the electrical power that imposed a cooling of ~20 K s⁻¹ between the experimental temperature and the fictive temperature of the melt. Although the experiment was terminated under a nominal isobaric quench mode of the apparatus, a rapid drop in pressure (<100 MPa) was observed following the turning off the electrical power. As such, the hydrous melt was subjected to fast cooling and decompression. For each experiment, we recovered material from the top, middle and bottom part of the capsule to check for sample homogeneity. The recovered samples were embedded in epoxy and polished for chemical, SEM and Raman spectroscopy analyses. The reproducibility of our results was tested by using different piston cylinder apparatuses at the Bayerisches Geoinstitut and by repeating the experiments up to six times for each apparatus.

Water content determination. Water content of glasses was measured using Fourier-transform infrared spectroscopy (FTIR). We used a Bruker IFS 120 spectrometer connected to a Bruker IR microscope. Spectra were acquired using a tungsten light source with a Si-coated CaF₂ beam-splitter and narrow-band MCT (mercury; cadmium; telluride) detector. FTIR measurements were acquired between 1000 and 6000 cm⁻¹ on doubly polished samples (~0.2–0.3 mm thickness). The analyzed spot was 100 μm in diameter with a spectral resolution of 4 cm⁻¹. For each spectrum, 200 scans were accumulated. All hydrous glasses were measured at least three times at different spots to account for heterogeneities.

Total water contents were derived from the peak areas of the OH⁻ and H₂O bands (~4500 and 5200 cm⁻¹, respectively), which corresponds to the combination of the stretching and bending modes. We used the “two Gaussians” (GG) baseline²⁰¹ and the “GGpar” integral molar absorption coefficients ($\epsilon_{OH^-} = 0.62$; $\epsilon_{H_2O_{mol}} = 0.71$)

following ref. ²⁰¹ and the density of glasses was calculated using ref. ¹³¹. For the ETN sample with the highest water content loaded before the synthesis (6.3 wt.%), FTIR estimation was not possible due to pervasive crystallization. Nevertheless, with Raman spectroscopy we estimated a minimum water content of 4.5 wt.% after ref. ⁶⁶.

Data availability

The raw data used for this study are publicly available online at <https://doi.org/10.6084/m9.figshare.21466452>.

Received: 31 May 2022; Accepted: 2 November 2022;

Published online: 18 November 2022

References

- Loughlin, S. C., Vye-Brown, C., Sparks, R. S. J., Brown, S. K. & Jenkins, S. *Global Volcanic Hazards and Risk* (Cambridge University Press, 2015).
- Baxter, P. J. Human impacts of volcanoes. in *Volcanoes and the Environment* 273–303 (Cambridge University Press, 2005). <https://doi.org/10.1017/CBO9780511614767.011>.
- McConnell, J. R. et al. Extreme climate after massive eruption of Alaska's Okmok volcano in 43 BCE and effects on the late Roman Republic and Ptolemaic Kingdom. *Proc. Natl. Acad. Sci. USA*. **117**, 15443–15449. <https://doi.org/10.1073/pnas.2002722117> (2020).
- Kandlbauer, J., Hopcroft, P. O., Valdes, P. J. & Sparks, R. S. J. Climate and carbon cycle response to the 1815 Tambora volcanic eruption. *J. Geophys. Res. Atmos.* **118**, 12497–12507 (2013).
- Auker, M. R., Sparks, R. S. J., Siebert, L., Croweller, H. S. & Ewert, J. A statistical analysis of the global historical volcanic fatalities record. *J. Appl. Volcanol.* **2**, 1–24 (2013).
- Newhall, C. G., Self, S. & Robock, A. Anticipating future Volcanic Explosivity Index (VEI) 7 eruptions and their chilling impacts. *Geosphere* **14**, 572–603 (2018).
- Oppenheimer, C. Climatic, environmental and human con sequences of the largest known historic eruption: Tambora volcano (Indonesia) 1815. *Prog. Phys. Geogr.* **27**, 230–259 (2003).
- Manga, M. et al. Volcanic eruptions and their repose, unrest, precursors, and timing. *Volcanic Eruptions and Their Repose, Unrest, Precursors, and Timing* (National Academies Press, 2017). <https://doi.org/10.17226/24650>.
- Melnik, O. & Sparks, R. S. J. Transient models of conduit flows during volcanic eruptions. in *Statistics in Volcanology* (eds Mader, H. M., Coles, S.G., Connor, C.B. & Connor, L. J.) 1–25 (The Geological Society of London, 2006).
- de' Michieli Vitturi, M., Clarke, A. B. B., Neri, A. & Voight, B. Transient effects of magma ascent dynamics along a geometrically variable dome-feeding conduit. *Earth Planet. Sci. Lett.* **295**, 541–553 (2010).
- La Spina, G., de' Michieli Vitturi, M. & Clarke, A. B. Transient numerical model of magma ascent dynamics: application to the explosive eruptions at the Soufrière Hills Volcano. *J. Volcanol. Geotherm. Res.* **336**, 118–139 (2017).
- Dufek, J. & Bergantz, G. W. Transient two-dimensional dynamics in the upper conduit of a rhyolitic eruption: A comparison of closure models for the granular stress. *J. Volcanol. Geotherm. Res.* **143**, 113–132 (2005).
- Rosi, M. et al. Defining the pre-eruptive states of active volcanoes for improving eruption forecasting. *Front. Earth Sci.* **10**, 1–20 (2022).
- Llewellin, E. W. & Manga, M. Bubble suspension rheology and implications for conduit flow. *J. Volcanol. Geotherm. Res.* **143**, 205–217 (2005).
- Vona, A., Romano, C., Dingwell, D. B. & Giordano, D. The rheology of crystal-bearing basaltic magmas from Stromboli and Etna. *Geochim. Cosmochim. Acta* **75**, 3214–3236 (2011).
- Mader, H. M., Llewellin, E. W. & Mueller, S. P. The rheology of two-phase magmas: a review and analysis. *J. Volcanol. Geotherm. Res.* **257**, 135–158 (2013).
- Dingwell, D. B. Volcanic dilemma: flow or blow? *Science* **273**, 1054–1055 (1996).
- Leshner, C. E. & Spera, F. J. Chapter 5 – Thermodynamic and transport properties of silicate melts and magma. in *The Encyclopedia of Volcanoes* 2nd edn (ed Sigurdsson, H.) 113–141 (Academic Press, 2015). <https://doi.org/10.1016/B978-0-12-385938-9.00005-5>.
- Lavallée, Y. & Kendrick, J. E. Chapter 5 – A review of the physical and mechanical properties of volcanic rocks and magmas in the brittle and ductile regimes. in *Forecasting and Planning for Volcanic Hazards, Risks, and Disasters. Hazards and Disasters Series*, Vol. 2 (ed Papale, P.) 153–238 (Elsevier, 2021).
- Dingwell, D. B., Romano, C. & Hess, K.-U. The effect of water on the viscosity of a haplogranitic melt under P-T-X conditions relevant to silicic volcanism. *Contrib. Mineral. Petrol.* **124**, 19–28 (1996).
- Di Genova, D. et al. A chemical tipping point governing mobilization and eruption style of rhyolitic magma. *Nature* **552**, 235–238 (2017).
- Richet, P., Lejeune, A. M., Holtz, F. & Roux, J. Water and the viscosity of andesite melts. *Chem. Geol.* **128**, 185–197 (1996).
- Liebske, C., Behrens, H., Holtz, F. & Lange, R. A. The influence of pressure and composition on the viscosity of andesitic melts. *Geochim. Cosmochim. Acta* **67**, 473–485 (2003).
- Whittington, A. G., Richet, P. & Holtz, F. Water and the viscosity of depolymerized aluminosilicate melts. *Geochim. Cosmochim. Acta* **64**, 3725–3736 (2000).
- Giordano, D. & Dingwell, D. B. Viscosity of hydrous Etna basalt: implications for Plinian-style basaltic eruptions. *Bull. Volcanol.* **65**, 8–14 (2003).
- Cassidy, M., Manga, M., Cashman, K. V. & Bachmann, O. Controls on explosive-effusive volcanic eruption styles. *Nat. Commun.* **9**, 2839 (2018).
- Gonnermann, H. M. & Manga, M. Dynamics of magma ascent in the volcanic conduit. in *Modeling Volcanic Processes: The Physics and Mathematics of Volcanism* (eds Fagents, S. A., Gregg, T. K. P. & Lopes, R. M. C.) 55 (Cambridge University Press, 2012).
- Giordano, D., Russell, J. K. & Dingwell, D. B. Viscosity of magmatic liquids: a model. *Earth Planet. Sci. Lett.* **271**, 123–134 (2008).
- Hui, H. & Zhang, Y. Toward a general viscosity equation for natural anhydrous and hydrous silicate melts. *Geochim. Cosmochim. Acta* **71**, 403–416 (2007).
- Duan, X. Model for calculating the viscosity of natural iron-bearing silicate melts over a wide range of temperatures, pressures, oxygen fugacities, and compositions. *Am. Mineral.* **99**, 2378–2388 (2014).
- Langhammer, D., Di Genova, D. & Steinle-Neumann, G. Modelling the viscosity of anhydrous and hydrous volcanic melt. *Geochem. Geophys. Geosyst.* **22**, e2021GC009918 (2021).
- Di Genova, D., Zandona, A. & Deubener, J. Unravelling the effect of nano-heterogeneity on the viscosity of silicate melts: implications for glass manufacturing and volcanic eruptions. *J. Non. Cryst. Solids* **545**, 120248 (2020).
- Kleest, C., Webb, S. L. & Fanara, S. Rheology of melts from the colli albiani volcanic district (Italy): a case study. *Contrib. Mineral. Petrol.* **175**, 82 (2020).
- Giordano, D. et al. Viscosity of Palmas-type magmas of the Paraná Magmatic Province (Rio Grande do Sul State, Brazil): implications for high-temperature silicic volcanism. *Chem. Geol.* **560**, 119981 (2021).
- Bouhifd, M. A., Richet, P., Besson, P., Roskosz, M. & Ingrin, J. Redox state, microstructure and viscosity of a partially crystallized basalt melt. *Earth Planet. Sci. Lett.* **218**, 31–44 (2004).
- Cassetta, M. et al. Estimating the viscosity of volcanic melts from the vibrational properties of their parental glasses. *Sci. Rep.* **11**, 13072. <https://doi.org/10.1038/s41598-021-92407-5> (2021).
- Barone, G. et al. Nanoscale surface modification of Mt. Etna volcanic ashes. *Geochim. Cosmochim. Acta* **174**, 70–84 (2016).
- Lerner, A. H. et al. Improving the reliability of Fe- and S- XANES measurements in silicate glasses: correcting beam damage and identifying Fe-oxide nanolites in hydrous and anhydrous melt inclusions. *Chem. Geo.* **586**, 120610 (2021).
- Hughes, E. C. et al. High spatial resolution analysis of the Iron oxidation state in silicate glasses using the electron probe. *Am. Mineral.* **103** (2018).
- Galoisy, L. & Georges, C. The unique speciation of iron in calc-alkaline obsidians. *Chem. Geol.* **559**, 119925. <https://doi.org/10.1016/j.chemgeo.2020.119925> (2020).
- Larre, C. et al. Particular H₂O dissolution mechanism in iron-rich melt: application to martian basaltic melt genesis. *J. Raman Spectrosc.* **51**, 493–507 (2020).
- Allabar, A., Gross, E. S. & Nowak, M. The effect of initial H₂O concentration on decompression – induced phase separation and degassing of hydrous phonolitic melt. *Contrib. Mineral. Petrol.* **2**, 1–19 (2020).
- Tacchetto, T. et al. Pre-nucleation geochemical heterogeneity within glassy anatectic inclusions and the role of water in glass preservation. *Contrib. Mineral. Petrol.* **176**, 1–19 (2021).
- Matsumoto, K. & Geshi, N. Shallow crystallization of eruptive magma inferred from volcanic ash microtextures: a case study of the 2018 eruption of Shinmoedake volcano, Japan. *Bull. Volcanol.* **83**, 1–14. <https://doi.org/10.1007/s00445-021-01451-6> (2021).
- Kennedy, E., Sari, B. & Scott, M. C. Chemical and structural alterations in the amorphous structure of obsidian due to nanolites. *Microsc. Microanal.* **28**, 1–7. <https://doi.org/10.1017/s1431927621013957> (2022).
- Knafelc, J. et al. Havre 2012 pink pumice is evidence of a short-lived, deep-sea, magnetite nanolite-driven explosive eruption. *Commun. Earth Environ.* **3**, 1–11 (2022).
- Di Genova, D. et al. In situ observation of nanolite growth in volcanic melt: a driving force for explosive eruptions. *Sci. Adv.* **6**, 1–13 (2020).
- Di Genova, D., Caracciolo, A. & Kolzenburg, S. Measuring the degree of “nanolitization” of volcanic glasses: understanding syn-eruptive processes recorded in melt inclusions. *Lithos* **318–319**, 209–218 (2018).

49. Cáceres, F. et al. Can nanolites enhance eruption explosivity? *Geology* **48**, 1–5 (2020).
50. Mujin, M. & Nakamura, M. A nanolite record of eruption style transition. *Geology* **42**, 611–614 (2014).
51. Mujin, M., Nakamura, M. & Miyake, A. Eruption style and crystal size distributions: crystallization of groundmass nanolites in the 2011 Shinmoedake eruption. *Am. Mineral* **102**, 2367–2380 (2017).
52. Geissman, J. W., Newberry, N. G. & Peacor, D. R. Discrete single-domain and pseudo-single-domain titanomagnetite particles in silicic glass of an ash-flow tuff. *Can. J. Earth Sci.* **20**, 334–338 (1983).
53. Schlinger, C. M. & Smith, R. M. Superparamagnetism in volcanic glasses of the KBS Tuff: transmission electron microscopy and magnetic behavior. *Geophys. Res. Lett.* **13**, 729–732 (1986).
54. Schlinger, C. M., Smith, R. M. & Veblen, D. R. Geologic origin of magnetic volcanic glasses in the KBS tuff. *Geology* **14**, 959–962 (1986).
55. Schlinger, C. M., Rosenbaum, J. G. & Veblen, D. R. Fe-oxide microcrystals in welded tuff from southern Nevada; origin of remanence carriers by precipitation in volcanic glass. *Geology* **16**, 556–559 (1988).
56. Schlinger, C. M., Scow, D. G. R., Papaefthymiou, G. C. & Veblen, D. R. The nature of magnetic single domains in volcanic glasses of the KBS Tuff minerals appear subsequent to the colorless shards have to a basic experiments and dark and optical variations in these particular rapidly cooled glasses separates of KBS shards. *J. Geophys. Res.* **93**, 9137–9156 (1988).
57. Eick, P. M. & Schlinger, C. M. The use of magnetic susceptibility and its frequency dependence for delineation of a magnetic stratigraphy in ash-flow tuffs. *Geophys. Res. Lett.* **17**, 783–786 (1990).
58. Schlinger, C. M., Veblen, D. R. & Rosenbaum, J. G. Magnetism and magnetic mineralogy of ash flow tuffs from Yucca Mountain, Nevada. *J. Geophys. Res.* **96**, 6035 (1991).
59. Stevenson, R. J., Dingwell, D. B., Webb, S. L. & Bagdassarov, N. S. The equivalence of enthalpy and shear stress relaxation in rhyolitic obsidians and quantification of the liquid-glass transition in volcanic processes. *J. Volcanol. Geotherm. Res.* **68**, 297–306 (1995).
60. Sharp, T. G., Stevenson, R. J. & Dingwell, D. B. Microlites and ‘nanolites’ in rhyolitic glass: microstructural and chemical characterization. *Bull. Volcanol.* **57**, 631–640 (1996).
61. Stevenson, R. J., Dingwell, D. B., Bagdassarov, N. S. & Manley, C. R. Measurement and implication of ‘effective’ viscosity for rhyolite flow emplacement. *Bull. Volcanol.* **63**, 227–237 (2001).
62. Platz, T., Cronin, S. J., Smith, I. E. M., Turner, M. B. & Stewart, R. B. Improving the reliability of microprobe-based analyses of andesitic glasses for tephra correlation. *The Holocene* **17**, 573–583 (2007).
63. Seaman, S. J., Dyar, M. D. & Marinkovic, N. The effects of heterogeneity in magma water concentration on the development of flow banding and spherulites in rhyolitic lava. *J. Volcanol. Geotherm. Res.* **183**, 157–169 (2009).
64. Burgess, K. D. et al. Submicrometer-scale spatial heterogeneity in silicate glasses using aberration-corrected scanning transmission electron microscopy. *Am. Mineral.* **101**, 2677–2688 (2016).
65. Shea, T. Bubble nucleation in magmas: a dominantly heterogeneous process? *J. Volcanol. Geotherm. Res.* **343**, 155–170 (2017).
66. Di Genova, D. et al. Effect of iron and nanolites on Raman spectra of volcanic glasses: reassessment of existing strategies to estimate the water content. *Chem. Geol.* **475**, 76–86 (2017).
67. Colombier, M. et al. Textural evolution of magma during the 9.4-ka trachytic explosive eruption at Kilian Volcano, Chaîne des Puys, France. *Bull. Volcanol.* **79**, 24 (2017).
68. Schiavi, F. et al. Water quantification in silicate glasses by Raman spectroscopy: Correcting for the effects of confocality, density and ferric iron. *Chem. Geol.* **483**, 312–331 (2018).
69. Ovalle, J. T. et al. Formation of massive iron deposits linked to explosive volcanic eruptions. *Sci. Rep.* **8**, 1–11 (2018).
70. Wilding, M. et al. Exploring the structure of glass-forming liquids using high energy X-ray diffraction, containerless methodology and molecular dynamics simulation. *J. Non-Crystalline Solids X* **3**, 100027 (2019).
71. Liedl, A. et al. A 3D imaging textural characterization of pyroclastic products from the 1538 AD Monte Nuovo eruption (Campi Flegrei, Italy). *Lithos* **340–341**, 316–331 (2019).
72. Hughes, E. C. et al. Low analytical totals in EPMA of hydrous silicate glass due to sub-surface charging: obtaining accurate volatiles by difference. **505**, 48–56 (2019).
73. Morrison, A. A. et al. Rheological investigation of lunar highland and mare impact melt simulants. *Icarus* **317**, 307–323 (2019).
74. Castilla, S. C. et al. Pre-eruptive conditions and pyroclastic emplacement of the last known vulcanian eruption of Azufral Volcano, SW Colombia. *J. South Am. Earth Sci.* **91**, 372–386 (2019).
75. Mujin, M. & Nakamura, M. Late-stage groundmass differentiation as a record of magma stagnation, fragmentation, and rewelding. *Bull. Volcanol.* **82**, 48 (2020).
76. Hughes, E. C. et al. The microanalysis of iron and sulphur oxidation states in silicate glass – understanding the effects of beam damage. in *IOP Conference Series: Materials Science and Engineering* 891 (2020).
77. Al-Mukadam, R., Di Genova, D., Bornhöft, H. & Deubener, J. High rate calorimetry derived viscosity of oxide melts prone to crystallization. *J. Non. Cryst. Solids* **536**, 119992 (2020).
78. Le Losq, C., Moretti, R., Oppenheimer, C., Baudelet, F. & Neuville, D. R. In situ XANES study of the influence of varying temperature and oxygen fugacity on iron oxidation state and coordination in a phonolitic melt. *Contrib. Mineral. Petrol.* **4**, 1–13 (2020).
79. Le Losq, C., Cicconi, M. R. & Neuville, D. R. Iron in silicate glasses and melts: implications for volcanological processes. *ESSOAr* 1–29. <https://doi.org/10.1002/essoar.10503261.1> (2020).
80. González-García, D., Giordano, D., Russell, J. K. & Dingwell, D. B. A Raman spectroscopic tool to estimate chemical composition of natural volcanic glasses. *Chem. Geol.* **556**, 119819 (2020).
81. Blundy, J. D. et al. Effect of redox on Fe-Mg-Mn exchange between olivine and melt and an oxybarometer for basalts. *Contributions to Mineralogy and Petrology* Vol. 7 (Springer Berlin Heidelberg, 2020).
82. Giordano, D. et al. Raman spectroscopy from laboratory and proximal to remote sensing: a tool for the volcanological sciences. *Remote Sens.* **12**, 805 (2020).
83. Lormand, C. et al. Slow ascent of unusually hot intermediate magmas triggering strombolian to sub-plinian eruptions. *J. Petrol.* **61**, egaa077 (2020).
84. Colombier, M. et al. Rheological change and degassing during a trachytic vulcanian eruption at Kilian Volcano, Chaîne des Puys, France. *Bull. Volcanol.* **82**, 463–463 (2020).
85. Burgisser, A., Arbaret, L., Martel, C., Forien, M. & Colombier, M. The role of oxides in the shallow vesiculation of ascending magmas. *J. Volcanol. Geotherm. Res.* **406**, 107072 (2020).
86. Romano, C. et al. Modelling and physico-chemical constraints to the 4.5 ka Agnano-Monte Spina Plinian eruption (Campi Flegrei, Italy). *Chem. Geol.* **532**, 119301 (2020).
87. Knafelc, J., Bryan, S. E., Gust, D. & Cathey, H. E. Defining pre-eruptive conditions of the Havre 2012 submarine rhyolite eruption using crystal archives. *Front. Earth Sci.* **8**, 310 (2020).
88. Sahagian, D. & Carley, T. L. Explosive volcanic eruptions and spinodal decomposition: a different approach to deciphering the tiny bubble paradox. *Geochem. Geophys. Geosyst.* **21**, 1–9. <https://doi.org/10.1029/2019GC008898> (2020).
89. Buono, G. et al. Dynamics of degassing in evolved alkaline magmas: petrological, experimental and theoretical insights. *Earth Sci. Rev.* **211**, 103402 (2020).
90. Samaniego, P. et al. Linking magmatic processes and magma chemistry during the post-glacial to recent explosive eruptions of Ubinas volcano (southern Peru). *J. Volcanol. Geotherm. Res.* **407**, 107095 (2020).
91. Giuliani, L. et al. Evolution of textures, crystal size distributions and growth rates of plagioclase, clinopyroxene and spinel crystallized at variable cooling rates from a mid-ocean ridge basaltic melt. *Earth Sci. Rev.* **204**, 103165 (2020).
92. Cáceres, F. et al. From melt to crystals: the effects of cooling on Fe-Ti oxide nanolites crystallisation and melt polymerisation at oxidising conditions. *Chem. Geol.* **563**, 120057 (2021).
93. González-García, D. et al. Retrieving dissolved H₂O content from micro-Raman spectroscopy on nanolitized silicic glasses: application to volcanic products of the Paraná Magmatic Province, Brazil. *Chem. Geol.* **567**, 120058 (2021).
94. Stabile, P. et al. The effect of iron and alkali on the nanocrystal-free viscosity of volcanic melts: a combined Raman spectroscopy and DSC study. *Chem. Geol.* **559**, 119991 (2021).
95. Nienhuis, E. T., Tuheen, M., Du, J. & McCloy, J. S. In situ pair distribution function analysis of crystallizing Fe-silicate melts. *J. Mater. Sci.* **56**, 5637–5657 (2021).
96. Rose-koga, E. F. et al. Silicate melt inclusions in the new millennium: a review of recommended practices for preparation, analysis, and data presentation. *Chem. Geol.* **570**, 120145 (2021).
97. Rotolo, S. G. et al. Volcanological evolution of Pantelleria Island (Strait of Sicily) peralkaline volcano: a review. *Comptes Rendus Géoscience—Sciences la Planète* **353**, 111–132 (2021).
98. Cabié, M., Neisius, T. & Blanc, W. Combined FIB/SEM tomography and TEM analysis to characterize high aspect ratio Mg-silicate particles inside silica-based optical fibres. *Mater. Charact.* **178**, 111261 (2021).
99. Liu, E. J. Magma behaving brittly. *Nat. Geosci.* **14**, 108–181. <https://doi.org/10.1038/s41561-021-00724-1> (2021).
100. Haag, M. B. et al. Multi-proxy case study of a Neoproterozoic rhyolite flow in southernmost Brazil: Emplacement mechanisms and implications for ancient felsic lavas. *J. South Am. Earth Sci.* **107**, 102982 (2021).

101. Hajimirza, S., Gonnermann, H. M. & Gardner, J. E. Reconciling bubble nucleation in explosive eruptions with geospeedometers. *Nat. Commun.* **12**, 1–8 (2021).
102. Giuliani, L. et al. Crystal-chemical variations of spinel, clinopyroxene, and plagioclase in MORB basaltic melt induced by continuous cooling. *Chem. Geol.* **594**, 120765 (2022).
103. Pereira, L. et al. A feedback mechanism between crystals and bubbles in a RuO₂-bearing melt. *J. Non-Cryst. Solids* **582**, 121456 (2022).
104. Yoshida, K., Tamura, Y. & Ono, S. Variety of the drift pumice clasts from the 2021 Fukutoku-Oka-no-Ba eruption, Japan. *Isl. Arc* **31**, 1–17. <https://doi.org/10.1111/iar.12441> (2022).
105. Pistone, M., Formo, E., Whittington, A. G., Herbst, T. & Cottrell, E. Direct nanoscale observations of degassing-induced crystallisation in felsic magmas. *Contrib. Mineral. Petrol.* **177**, 38 (2022).
106. Jones, T. J., Cashman, K. V., Liu, E. J., Rust, A. C. & Scheu, B. Magma fragmentation: a perspective on emerging topics and future directions. *Bull. Volcanol.* **84**, 45 (2022).
107. Kurokawa, A. K., Miwa, T. & Ishibashi, H. Aging in magma rheology. *Sci. Rep.* **12**, 10015 (2022).
108. Okumura, S. H., Mujin, M., Tsuchiyama, A. & Miyake, A. 3D crystal size distributions of pyroxene nanolites from nano X-ray computed tomography: improved correction of crystal size distributions from CSDCorrections for magma ascent dynamics in conduits. *Am. Mineral* **107**, 1766–1778 (2022).
109. Jordanova, D. et al. A detailed magnetic record of Pleistocene climate and distal ash dispersal during the last 800 kyrs – The Suhia Kladenetz quarry loess-paleosol sequence near Pleven (Bulgaria). *Glob. Planet. Change* **214**, 103840 (2022).
110. Vigliotti, L., Bilardello, D., Winkler, A. & Del Carlo, P. Rock magnetic fingerprint of Mt Etna volcanic ash. *Geophys. J. Int.* **231**, 749–769 (2022).
111. Dubosq, R. et al. Bubbles and atom clusters in rock melts: a chicken and egg problem. *J. Volcanol. Geotherm. Res.* **428**, 107574 (2022).
112. Jones, T. J. et al. Inflated pyroclasts in proximal fallout deposits reveal abrupt transitions in eruption behaviour. *Nat. Commun.* **13**, 1–12 (2022).
113. Branca, S. & Del Carlo, P. Types of eruptions of Etna volcano AD 1670–2003: Implications for short-term eruptive behaviour. *Bull. Volcanol.* **67**, 732–742 (2005).
114. Corsaro, R. A. et al. Monitoring the December 2015 summit eruptions of Mt. Etna (Italy): Implications on eruptive dynamics. *J. Volcanol. Geotherm. Res.* **341**, 53–69 (2017).
115. Polacci, M., Corsaro, R. A. & Andronico, D. Coupled textural and compositional characterization of basaltic scoria: Insights into the transition from Strombolian to fire fountain activity at Mount Etna, Italy. *Geology* **34**, 201–204 (2006).
116. Andronico, D., Cristaldi, A., Del Carlo, P. & Taddeucci, J. Shifting styles of basaltic explosive activity during the 2002–03 eruption of Mt. Etna, Italy. *J. Volcanol. Geotherm. Res.* **180**, 110–122 (2009).
117. Alparone, S., Andronico, D., Lodato, L. & Sgroi, T. Relationship between tremor and volcanic activity during the Southeast Crater eruption on Mount Etna in early 2000. *J. Geophys. Res.* **108**, 2241 (2003).
118. Andronico, D., Cristaldi, A. & Scollo, S. The 4–5 September 2007 lava fountain at South-East Crater of Mt Etna, Italy. *J. Volcanol. Geotherm. Res.* **173**, 325–328 (2008).
119. Barsotti, S. et al. Quantitative assessment of volcanic ash hazards for health and infrastructure at Mt. Etna (Italy) by numerical simulation. *J. Volcanol. Geotherm. Res.* **192**, 85–96 (2010).
120. Calvari, S., Cannavò, F., Bonaccorso, A., Spampinato, L. & Pellegrino, A. G. Paroxysmal explosions, lava fountains and ash plumes at Etna Volcano: eruptive processes and hazard implications. *Front. Earth Sci.* **6**, 107 (2018).
121. Wilson, L., Parfitt, E. A. & Head, J. W. Explosive volcanic eruptions—VIII. The role of magma recycling in controlling the behaviour of Hawaiian-style lava fountains. *Geophys. J. Int.* **121**, 215–225 (1995).
122. Giuffrida, M., Viccaro, M. & Ottolini, L. Ultrafast syn-eruptive degassing and ascent trigger high-energy basic eruptions. *Sci. Rep.* **8**, 147 (2018).
123. Calvari, S. et al. Lava effusion—a slow fuse for paroxysms at Stromboli volcano? *Earth Planet. Sci. Lett.* **301**, 317–323 (2011).
124. Carbone, D., Zuccarello, L., Messina, A., Scollo, S. & Rymer, H. Balancing bulk gas accumulation and gas output before and during lava fountaining episodes at Mt. Etna. *Sci. Rep.* **5**, 1–11 (2015).
125. Calvari, S. Multidisciplinary approach yields insight into Mt. Etna eruption. *Eos (Washington, DC)* **82**, 653–656 (2001).
126. La Spina, G. et al. Explosivity of basaltic lava fountains is controlled by magma rheology, ascent rate and outgassing. *Earth Planet. Sci. Lett.* **1**, 116658 (2021).
127. James, M. R., Lane, S. J. & Chouet, B. Gas slug ascent through changes in conduit diameter: laboratory insights into a volcano-seismic source process in low-viscosity magmas. *J. Geophys. Res.* **111**, B05201 (2006).
128. Chouet, B., Dawson, P. & Martini, M. Shallow-conduit dynamics at Stromboli Volcano, Italy, imaged from waveform inversions. in *Fluid Motions in Volcanic Conduits: A Source of Seismic and Acoustic Signals* (Geological Society of London, 2008). <https://doi.org/10.1144/SP307.5>.
129. Bertagnini, A., Di Roberto, A. & Pompilio, M. Paroxysmal activity at Stromboli: lessons from the past. *Bull. Volcanol.* **73**, 1229–1243 (2011).
130. Barberi, F., Rosi, M. & Sodi, A. Volcanic hazard assessment at Stromboli based on review of historical data. *Acta Vulcanol* **3**, 173–187 (1993).
131. Misiti, V. et al. Viscosity of high-K basalt from the 5th April 2003 Stromboli paroxysmal explosion. *Chem. Geol.* **260**, 278–285 (2009).
132. Giordano, G. & De Astis, G. The summer 2019 basaltic Vulcanian eruptions (paroxysms) of Stromboli. *Bull. Volcanol.* **83**, 1 (2021).
133. Viccaro, M. et al. Shallow conduit dynamics fuel the unexpected paroxysms of Stromboli volcano during the summer 2019. *Sci. Rep.* **11**, 1–15 (2021).
134. Andronico, D. et al. Uncovering the eruptive patterns of the 2019 volcano. *Nat. Commun.* **12**, 1–14. <https://doi.org/10.1038/s41467-021-24420-1> (2021).
135. Métrich, N., Bertagnini, A. & Pistolesi, M. Paroxysms at Stromboli Volcano (Italy): source, genesis and dynamics. *Front. Earth Sci.* **9**, 1–17 (2021).
136. Pichavant, M., Di Carlo, I., Le Gac, Y., Rotolo, S. G. & Scaillet, B. Experimental constraints on the deep magma feeding system at Stromboli Volcano, Italy. *J. Petrol.* **50**, 601–624 (2009).
137. Le Gall, N. & Pichavant, M. Experimental simulation of bubble nucleation and magma ascent in basaltic systems: implications for Stromboli volcano. *Am. Mineral.* **101**, 1967–1985 (2016).
138. Cimarelli, C., Di Traglia, F. & Taddeucci, J. Basaltic scoria textures from a zoned conduit as precursors to violent Strombolian activity. *Geology* **38**, 439–442 (2010).
139. Oppenheimer, J. et al. Analogue experiments on the rise of large bubbles through a solids-rich suspension: a “weak plug” model for Strombolian eruptions. *Earth Planet. Sci. Lett.* **531**, 115931 (2020).
140. Mauro, J. C., Yue, Y. Z., Ellison, A. J., Gupta, P. K. & Allan, D. C. Viscosity of glass-forming liquids. *Proc. Natl. Acad. Sci. USA.* **106**, 19780–19784 (2009).
141. Zheng, Q., Mauro, J. C., Ellison, A. J., Potuzak, M. & Yue, Y. Universality of the high-temperature viscosity limit of silicate liquids. *Phys. Rev. B Condens. Matter Mater. Phys.* **83**, 13–15 (2011).
142. Giordano, D. et al. The rheological evolution of alkaline Vesuvius magmas and comparison with alkaline series from the Phlegrean Fields, Etna, Stromboli and Teide. *Geochim. Cosmochim. Acta* **73**, 6613–6630 (2009).
143. Di Muro, A. et al. Micro-Raman determination of iron redox state in dry natural glasses: application to peralkaline rhyolites and basalts. *Chem. Geol.* **259**, 78–88 (2009).
144. Di Genova, D. et al. Raman spectra of Martian glass analogues: a tool to approximate their chemical composition. *J. Geophys. Res. Planets* **121**, 740–752 (2016).
145. McMillan, P. F. Structural studies of silicate glasses and melts—applications and limitations of Raman spectroscopy. *Am. Mineral.* **69**, 622–644 (1984).
146. de Faria, D. L. A., Silva, S. V. & de Oliveira, M. T. Raman microspectroscopy of some iron oxides and oxyhydroxides. *J. Raman Spectrosc.* **28**, 873–878 (1997).
147. Zandona, A., Groß, C. B. M., Rüdinger, B. & Deubener, J. A threshold heating rate for single-stage heat treatments in glass-ceramics containing seed formers. *J. Am. Ceram. Soc.* **104**, 4433–4444 (2021).
148. Bhattacharyya, S. et al. Direct evidence of Al-rich layers around nanosized ZrTiO₄ in glass: putting the role of nucleation agents in perspective. *Cryst. Growth Des.* **10**, 379–385 (2010).
149. Kleebusch, E., Patzig, C., Höche, T. & Rüssel, C. The evidence of phase separation droplets in the crystallization process of a Li₂O–Al₂O₃–SiO₂ glass with TiO₂ as nucleating agent – An X-ray diffraction and (S)TEM-study supported by EDX-analysis. *Ceram. Int.* **44**, 2919–2926 (2018).
150. Kleebusch, E. et al. The formation of nanocrystalline ZrO₂ nuclei in a Li₂O–Al₂O₃–SiO₂ glass – a combined XANES and TEM study. *Sci. Rep.* **7**, 1–12 (2017).
151. Fotheringham, U., Wurth, R. & Rüssel, C. Thermal analyses to assess diffusion kinetics in the nano-sized interspaces between the growing crystals of a glass ceramics. *Thermochim. Acta* **522**, 144–150 (2011).
152. Höche, T. et al. Temporal evolution of diffusion barriers surrounding ZrTiO₄ nuclei in lithia aluminosilicate glass-ceramics. *Cryst. Growth Des.* **12**, 1556–1563 (2012).
153. Mitchell, A. L. et al. Nanoscale microstructure and chemistry of transparent gahnite glass-ceramics revealed by atom probe tomography. *Scr. Mater.* **203**, 114110 (2021).
154. Zandona, A., Patzig, C., Rüdinger, B., Hochrein, O. & Deubener, J. TiO₂(B) nanocrystals in Ti-doped lithium aluminosilicate glasses. *J. Non-Crystalline Solids X* **2**, 100025 (2019).
155. Conte, A. M., Perinelli, C. & Trigila, R. Cooling kinetics experiments on different Stromboli lavas: effects on crystal morphologies and phases composition. *J. Volcanol. Geotherm. Res.* **155**, 179–200 (2006).
156. Ryerson, F. J. & Watson, E. B. Rutile saturation in magmas: implications for Ti–Nb–Ta depletion in island-arc basalts. *Earth Planet. Sci. Lett.* **86**, 225–239 (1987).

157. Ayers, J. C. et al. The solubility of titanite in silicate melt determined from growth and dissolution experiments. *Contrib. Mineral. Petrol.* **177**, 37 (2022).
158. Gaetani, G. A., Asimow, P. D. & Stolper, E. M. A model for rutile saturation in silicate melts with applications to eclogite partial melting in subduction zones and mantle plumes. *Earth Planet. Sci. Lett.* **272**, 720–729 (2008).
159. Andreeva, O. A. et al. Silicate liquid immiscibility as a result of Fenner-type crystal fractionation of Wangtian'e Tholeiitic Melts, Northeast China. *Petrology* **28**, 357–373 (2020).
160. Hill, R. & Roeder, P. The crystallization of spinel from basaltic liquid as a function of oxygen fugacity. *J. Geol.* **82**, 709–729 (1974).
161. Toplis, M. J. & Carroll, M. R. An experimental study of the influence of oxygen fugacity on Fe-Ti oxide stability, phase relations, and mineral-melt equilibria in ferro-basaltic systems. *J. Petrol.* **36**, 1137–1170 (1995).
162. Hrma, P. Crystallization during processing of nuclear waste glass. *J. Non. Cryst. Solids* **356**, 3019–3025 (2010).
163. Zandonà, A. et al. Glass-forming ability and ZrO₂ saturation limits in the magnesium aluminosilicate system. *Ceram. Int.* **48**, 8433–8439 (2022).
164. Zandonà, A. et al. Glass formation and devitrification behavior of alkali (Li, Na) aluminosilicate melts containing TiO₂. *J. Non. Cryst. Solids* **582**, 121448 (2022).
165. Hurwitz, S. & Navon, O. Bubble nucleation in rhyolitic melts: experiments at high pressure, temperature, and water content. *Earth Planet. Sci. Lett.* **122**, 267–280 (1994).
166. Mangan, M. T., Sisson, T. W. & Hankins, W. B. Decompression experiments identify kinetic controls on explosive silicic eruptions. *Geophys. Res. Lett.* **31**, 1–5 (2004).
167. Larsen, J. F. Heterogeneous bubble nucleation and disequilibrium H₂O exsolution in Vesuvius K-phonolite melts. *J. Volcanol. Geotherm. Res.* **175**, 278–288 (2008).
168. Knipping, J. L., Webster, J. D., Simon, A. C. & Holtz, F. Accumulation of magnetite by flotation on bubbles during decompression of silicate magma. *Sci. Rep.* **9**, 1–7 (2019). 3852.
169. Pleše, P. et al. Production and detachment of oxide crystal shells on bubble walls during experimental vesiculation of andesitic magmas. *Contrib. Mineral. Petrol.* **174**, 21 (2019).
170. La Spina, G., Burton, M. R., de' Michieli Vitturi, M. & Arzilli, F. Role of syn-eruptive plagioclase disequilibrium crystallization in basaltic magma ascent dynamics. *Nat. Commun.* **7**, 13402 (2016).
171. Arzilli, F. et al. Magma fragmentation in highly explosive basaltic eruptions induced by rapid crystallization. *Nat. Geosci.* **12**, 1023–1028 (2019).
172. Polacci, M. et al. The role of syn-eruptive vesiculation on explosive basaltic activity at Mt. Etna, Italy. *J. Volcanol. Geotherm. Res.* **179**, 265–269 (2009).
173. Colombier, M. et al. Degassing and gas percolation in basaltic magmas. *Earth Planet. Sci. Lett.* **573**, 117134 (2021).
174. Namiki, A. & Manga, M. Transition between fragmentation and permeable outgassing of low viscosity magmas. *J. Volcanol. Geotherm. Res.* **169**, 48–60 (2008).
175. Valdivia, P., Marshall, A. A., Brand, B. D., Manga, M. & Huber, C. Mafic explosive volcanism at Llaima Volcano: 3D x-ray microtomography reconstruction of pyroclasts to constrain shallow conduit processes. *Bull. Volcanol.* **84**, 2. <https://doi.org/10.1007/s00445-021-01514-8> (2022).
176. Mueller, S., Melnik, O., Spieler, O., Scheu, B. & Dingwell, D. B. Permeability and degassing of dome lavas undergoing rapid decompression: an experimental determination. *Bull. Volcanol.* **67**, 526–538 (2005).
177. Bamber, E. C. et al. Pre- and syn-eruptive conditions of a basaltic Plinian eruption at Masaya Volcano, Nicaragua: The Masaya Triple Layer (2.1 ka). *J. Volcanol. Geotherm. Res.* **392**, 106761 (2020).
178. Szramek, L. Mafic Plinian eruptions: is fast ascent required? *J. Geophys. Res. Solid Earth* **121**, 7119–7136. <https://doi.org/10.1002/2016JB013208> (2016).
179. Coltelli, M., Del Carlo, P. & Vezzoli, L. Discovery of a Plinian basaltic eruption of Roman age at Etna volcano, Italy. *Geology* **26**, 1095–1098 (1998).
180. Costantini, L., Houghton, B. F. & Bonadonna, C. Constraints on eruption dynamics of basaltic explosive activity derived from chemical and microtextural study: the example of the Fontana Lapilli Plinian eruption, Nicaragua. *J. Volcanol. Geotherm. Res.* **189**, 207–224 (2010).
181. Rowe, M. C. et al. Tarawera 1886: an integrated review of volcanological and geochemical characteristics of a complex basaltic eruption. *New Zeal. J. Geol. Geophys.* **64**, 296–319 (2021).
182. Marshall, A. A. et al. The mafic Curacautín ignimbrite of Llaima volcano, Chile. *J. Volcanol. Geotherm. Res.* **421**, 107418 (2022).
183. Le Gall, N. et al. In situ quantification of crystallisation kinetics of plagioclase and clinopyroxene in basaltic magma: implications for lava flow. *Earth Planet. Sci. Lett.* **568**, 117016 (2021).
184. Arzilli, F. et al. Dendritic crystallization in hydrous basaltic magmas controls magma mobility within the Earth's crust. *Nat. Commun.* **13**, 3354 (2022).
185. Al-Mukadam, R., Götz, I. K., Stolpe, M. & Deubener, J. Viscosity of metallic glass-forming liquids based on Zr by fast-scanning calorimetry. *Acta Mater* **221**, 117370 (2021).
186. Schawe, J. E. K. & Hess, K.-U. The kinetics of the glass transition of silicate glass measured by fast scanning calorimetry. *Thermochim. Acta* **677**, 85–90 (2019).
187. Behncke, B. & Neri, M. The July–August 2001 eruption of Mt. Etna (Sicily). *Bull. Volcanol.* **65**, 461–476 (2003).
188. Landi, P. et al. Magma dynamics during the 2007 Stromboli eruption (Aeolian Islands, Italy): mineralogical, geochemical and isotopic data. *J. Volcanol. Geotherm. Res.* **182**, 255–268 (2009).
189. Di Fiore, F., Vona, A., Kolzenburg, S., Mollo, S. & Romano, C. An extended rheological map of Pāhoehoe—'A'ā Transition. *J. Geophys. Res. Solid Earth* **126**, 1–23 (2021).
190. Di Fiore, F., Vona, A., Costa, A., Mollo, S. & Romano, C. Quantifying the influence of cooling and shear rate on the disequilibrium rheology of a trachybasaltic melt from Mt. Etna. *Earth Planet. Sci. Lett.* **594**, 117725 (2022).
191. Di Fiore, F. et al. Kinetic partitioning of major and trace cations between clinopyroxene and phonotephritic melt under convective stirring conditions: New insights into clinopyroxene sector zoning and concentric zoning. *Chem. Geol.* **584**, 120531 (2021).
192. Meerlender, G. Viskositäts-Temperaturverhalten des Standardglases I der DGG. *Glas. Ber.* **47**, 1–3 (1974).
193. Deubener, J. et al. Viscosity, relaxation and elastic properties of photo-thermo-refractive glass. *J. Non. Cryst. Solids* **355**, 126–131 (2009).
194. Behrens, H. et al. Structural relaxation mechanisms in hydrous sodium borosilicate glasses. *J. Non. Cryst. Solids* **497**, 30–39 (2018).
195. Di Genova, D., Romano, C., Alletti, M., Misiti, V. & Scarlato, P. The effect of CO₂ and H₂O on Etna and Fondo Riccio (Phlegrean Fields) liquid viscosity, glass transition temperature and heat capacity. *Chem. Geol.* **377**, 72–86 (2014).
196. Douglas, R. W., Armstrong, W. L., Edward, J. & Hall, D. A penetration viscometer. *Glas. Technol.* **6**, 52–55 (1965).
197. Al-Mukadam, R., Zandonà, A. & Deubener, J. Kinetic fragility of pure TeO₂ glass. *J. Non. Cryst. Solids* **554**, 1–6 (2021).
198. Scarani, A. et al. Determination of cooling rates of glasses over four orders of magnitude. *Contrib. Mineral. Petrol.* **177**, 1–17 (2022).
199. Rustioni, G., Audétat, A. & Keppler, H. The composition of subduction zone fluids and the origin of the trace element enrichment in arc magmas. *Contrib. Mineral. Petrol.* **176**, 51 (2021).
200. Audétat, A., Miyajima, N., Wiesner, D. & Audinot, J.-N. Confirmation of slow Ti diffusion in quartz by diffusion couple experiments and evidence from natural samples. *Geology* **49**, 963–967 (2021).
201. Ohlhorst, S., Behrens, H. & Holtz, F. Compositional dependence of molar absorptivities of near-infrared OH- and H₂O bands in rhyolitic to basaltic glasses. *Chem. Geol.* **174**, 5–20 (2001).

Acknowledgements

A.S., F.D.F., A.V. and C.R. acknowledge the Grant of Excellence Departments, MIUR-Italy (ARTICOLO 1, COMMI 314 – 337 LEGGE 232/2016). D.D.G. and P.V. acknowledge funding by Deutsche Forschungsgemeinschaft (DFG) project DI 2751/2–1. A.Z. also acknowledges the DFG for funding his research through the Walter Benjamin Program, grant no. 448961237, ZA 1188/1–1. The TEM facility at Bayerisches Geoinstitut is supported by DFG grant INST 91/251-1 FUGG.

Author contributions

Conceptualization: A.S., A.Z., F.D.F., A.V., D.D.G. Funding acquisition: A.Z., A.V., N.M., C.R., D.D.G. Investigation: A.S., A.Z., F.D.F., P.V., N.M., H.B., R.P. Methodology: A.S., A.Z., F.D.F., A.V., P.V., N.M., D.D.G. Resources: N.M., J.D., C.R. Supervision: D.D.G. and A.V. Visualization: A.S., A.Z., N.M., R.P. Writing—original draft: D.D.G., A.Z., A.S., A.V. Writing—review and editing: A.S., A.Z., F.D.F., P.V., N.M., H.B., A.V., J.D., C.R., D.D.G.

Competing interests

The authors declare no competing interests.

Additional information

Supplementary information The online version contains supplementary material available at <https://doi.org/10.1038/s43247-022-00615-2>.

Correspondence and requests for materials should be addressed to Alex Scarani or Alessio Zandonà.

Peer review information *Communications Earth & Environment* thanks the anonymous reviewers for their contribution to the peer review of this work. Primary Handling Editor: Joe Aslin. Peer reviewer reports are available.

Reprints and permission information is available at <http://www.nature.com/reprints>

Publisher's note Springer Nature remains neutral with regard to jurisdictional claims in published maps and institutional affiliations.



Open Access This article is licensed under a Creative Commons Attribution 4.0 International License, which permits use, sharing, adaptation, distribution and reproduction in any medium or format, as long as you give appropriate credit to the original author(s) and the source, provide a link to the Creative Commons license, and indicate if changes were made. The images or other third party material in this article are included in the article's Creative Commons license, unless indicated otherwise in a credit line to the material. If material is not included in the article's Creative Commons license and your intended use is not permitted by statutory regulation or exceeds the permitted use, you will need to obtain permission directly from the copyright holder. To view a copy of this license, visit <http://creativecommons.org/licenses/by/4.0/>.

© The Author(s) 2022